

High Constriction Ratio Continuous
Insulator Based Dielectrophoretic Particle Sorting

by

Qianru Wang

B.S., Shanghai Jiao Tong University (2012)

Submitted to the Department of Mechanical Engineering
in partial fulfillment of the requirements for the degree of

Master of Science in Mechanical Engineering

at the

Massachusetts Institute of Technology

September 2014

© 2014 Massachusetts Institute of Technology. All rights reserved

Signature redacted

Signature of Author.....

Department of Mechanical Engineering

August 25, 2014

Signature redacted

Certified by.....

Cullen R. Buie

Assistant Professor

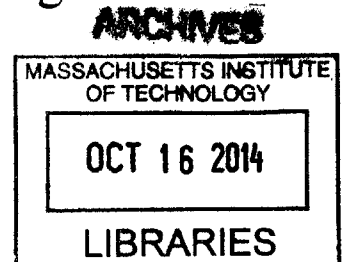
Thesis Supervisor

Signature redacted

Accepted by.....

David E. Hardt

Graduate Officer, Department of Mechanical Engineering



High Constriction Ratio Continuous Insulator Based Dielectrophoretic Particle Sorting

by

Qianru Wang

Submitted to the Department of Mechanical Engineering
on August 25, 2014, in partial fulfillment of the
requirements for the degree of
Master of Science in Mechanical Engineering

Low frequency insulator based dielectrophoresis (iDEP) is a promising technique to study cell surface dielectric properties. To date, iDEP has been exploited to distinguish, characterize, and manipulate particles and bacteria based on their size and general cell phenotype (e.g. gram positive vs. gram negative). However, separation of bacteria with diverse surface phenotypes but similar sizes sets a much higher demand on separation sensitivity, necessitating improvement in channel structure design in order to increase the electrical field gradient. In this work, a three dimensional insulator based dielectrophoresis (3DiDEP) microdevice is designed to achieve continuous particle sorting based on their size and, more importantly, on their surface dielectric properties. A 3D constriction is fabricated inside Poly (methyl methacrylate) (PMMA) channels using a micromilling technique. By controlling the channel geometry at the 3D constriction area, a nonuniform electric field with a large intensity gradient perpendicular to the local particle flow direction results in transverse particle deflection, driving particles into different outlet streams. With both simulation and experiments, we show that a diverse array of particles can be distinguished by 3DiDEP. This 3DiDEP sorter can be used in multiple applications in which the surface properties of cells or particles are of special interest.

Thesis Supervisor: Cullen R. Buie

Title: Assistant Professor

Acknowledgements

I would like to express my deepest appreciation to my advisor, Professor Cullen Buie, who has provided constant guidance and support to me throughout this work and conveyed spirits of persistence and seeking the truth. My successful transition from my undergraduate focus on mechanical design and manufacturing to the microfluidics incorporating biology and electrokinetics would not have been possible without his help.

I also would like to thank Dr. William Braff, a recent alumnus of Prof. Buie's group, for his guidance in helping me to start this project. I have learned a lot from his experience with DEP-based microfluidic systems, and obtained a great deal of inspiration from our discussions.

I am also thankful to the other members of the Laboratory for Energy and Microsystems Innovation (LEMI), including Wai Hong Ronald Chan, Naga N. Dingari, Dr. Paulo A. Garcia, Zhifei Ge, Laura M. Gilson, Gregoire Jacquot, Andrew D. Jones, Dr. Youngsoo Joung, Dr. Jeffrey L. Moran, Alisha Schor, and Dr. Matthew Suss. They are excellent engineers and gave me a lot of valuable advice and assistance over the past two years. I would like to thank Dr. Pei Zhang, a former postdoctoral researcher in LEMI, for her advice on biology-related topics.

I must pay special thanks to my dear parents, Yuxing Wang and Yanqin Tang, for their persistent encouragement and support from China. Their consistent understanding and support breathe strength, confidence and a positive attitude into my work.

Contents

1 Introduction	13
1.1 Cell sorting on microfluidic chips	13
1.2 Dielectrophoresis	14
1.3 Cell phenotype screening	15
1.4 Organization	16
2 Principles of Dielectrophoresis	19
2.1 Introduction	19
2.2 Field induced dielectric polarization and DEP	19
2.3 Scaling of the relaxation time	22
2.4 Dielectric cell model	24
3 3DiDEP Sorter Design and Fabrication	31
3.1 Introduction	31
3.2 Design of 3DiDEP channel geometry	31
3.3 Microfabrication of 3DiDEP devices	32
4 Analysis of 3DiDEP based particle separation	35
4.1 Introduction	35
4.2 Governing equations and assumptions	36
4.2.1 Electric field	36
4.2.2 Flow field	36
4.2.3 Temperature field	37

4.2.4 Particle motion near the constriction.....	38
4.3 Channel geometry factor χ	39
4.3.1 Serial electric resistor model	39
4.3.2 Parallel hydraulic resistor model.....	42
4.3.3 Criteria of 3DiDEP particle separation.....	44
4.4 Numerical modeling.....	46
4.4.1 Prediction of particle trajectories.....	46
4.4.2 Prediction of electrothermal flow	51
5 Continuous separation of particles based on size.....	57
5.1 Introduction	57
5.2 Methods and procedures.....	57
5.3 3DiDEP device assessment with polystyrene microspheres	60
6 Conclusion and future work	63
A Design of the 3DiDEP microfluidic device for continuous particle separation (machined PMMA surface).....	65
B Machine code for 3DiDEP microdevice.....	67
Bibliography.....	75

List of Figures

Figure 1-1	Overview of continuous cell separation using 3DiDEP	16
Figure 2-1	Diagrams of (a) the ellipsoid two-shell model considered for <i>E. coli</i> cells and (b) the homogeneous spherical model for polystyrene beads. Variation of the real part of Clausius-Mossotti factor of (c) <i>E. coli</i> 5K ¹⁵ and (d) polystyrene beads ⁷³ with changes in the medium conductivity (in S/m)	29
Figure 3-1	Design of the 3DiDEP microdevice.	32
Figure 3-2	Tool length measurement calibration for 50 and 100 μm end mills	34
Figure 4-1	Schematic of forces experienced by particles in the vicinity of the constriction...	38
Figure 4-2	Schematic for the serial electric resistor model to evaluate the impact of the insulating channel geometry on the electric field distribution	40
Figure 4-3	Relationship between the normalized y-component of $\nabla E^2 $ and the effective constriction ratio squared	42
Figure 4-4	Schematic for the parallel hydraulic resistor model to evaluate the impact of the insulating channel geometry on the fluid field	43
Figure 4-5	Sorting parameter calculated for particles with diameters of 6 μm (blue) and 1 μm (red)	46
Figure 4-6	Meshed computational domain with labeled surface and boundaries	47
Figure 4-7	COMSOL simulation results showing the 2D distribution of the electric field (a) and the flow field (b) on the center horizontal plane of the constriction. (c) 3D trajectory prediction for polystyrene beads with diameters of 6 μm (red) and 1 μm (blue)	50
Figure 4-8	(a) Isometric view of the labeled computational domains and boundaries of the 3D electrothermal flow model. (b) Volumetric RMS voltage distribution when a 100 V difference is applied across a microchannel.	52

Figure 4-9	Temperature change (ΔT) along the microchannel with various voltages applied	54
Figure 4-10	Streamlines of the fluid flow (solid lines) and distribution of velocity magnitude (color scale) when applied with RMS voltage differences of 50 V (a, b), 100 V(c, d) and 150 V (e, f). The cases of pure electrothermal flow are shown in (a, c, and e), while the interplayed cases involving both the pressure driven flow and the electrothermal flow are demonstrated in (b, d, and f)	55
Figure 5-1	(a) Experimental setup for 3DiDEP particle sorting. (b) Photograph of a 3DiDEP chip with an array of three microchannels. (c) Micrograph of the 3DiDEP channel geometry.	59
Figure 5-2	Fluorescence time-lapse image sequences for motion of (a-c) 6 μm beads, (d-f) 1 μm beads, and (g-i) both large (red) and small (green) beads in the mixture near the constriction region. Each experiment was conducted in triplicate under a 500 Hz AC signal with root mean square voltages of (a, d, and g) 64 V, (b, e, and h) 81 V, and (c, f, and i) 99V	61
Figure 5-3	Sorting efficiency parameter α calculated from (a) experiments conducted with 6 μm beads (red) and 1 μm beads (green) separately, and (b) experiments conducted with a mixture of large (red) and small (green) beads.	62

List of Tables

Table 2.1	Parameters for the calculation of Clausius-Mossotti factor	28
Table 4.1	Constants and parameters used in the 3DiDEP numerical model	48
Table 4.2	Boundary conditions for the stationary step of the particle trajectory model	49

Chapter 1

Introduction

1.1 Cell sorting on microfluidic chips

The ability to distinguish homogeneous cell populations from a heterogeneous cell mixture with high efficiency and sensitivity plays a significant role for accurate biochemical study, allowing for the underlying analysis and subsequent cultivation of defined cell populations. Existing traditional cell sorting methods can be separated into two main categories. The first is the physical separation method including filtration and centrifugation techniques^{63, 17, 61} that fractionate cells based on physical properties such as size, shape, and density. The second group is based on affinity methods like cell capture on an affinity solid matrix (immunoabsorbents),^{23, 22} fluorescence-activated cell sorting (FACS),^{36, 28} and magnetic-activated cell sorting (MACS).⁶⁵ The former method is mainly utilized as a debulking step followed by the affinity based separation of rare cell subtypes. Although the aforementioned methods are already widely used and commercialized,²¹ there are some drawbacks that are worth mentioning. For instance, FACS and MACS both involve the modification of cell membrane, and thus are no longer preferable for analysis and cell re-cultivation.⁶⁹ In addition, the chromatography of living cells using immunoabsorbents has a common problem of low yield due to the difficulties of achieving high recovery of bound cells without effecting their viability and functions.⁹ To date, due to the advancement of micro fabrication techniques, microfluidic systems are increasingly implemented in biomedical research, and the application of AC electrokinetic forces, in particular dielectrophoresis (DEP), to control and manipulate bioparticles, such as bacteria, cells, viruses, and DNA in suspension is now possible.²⁴ Compared with conventional cell isolation techniques, microfluidic devices provide rapid and portable measurements on small sample volumes while avoiding the need for labor-intensive operations. More importantly, successful implementations of DEP based microfluidic systems open the possibility to achieve label-free high sensitivity cell separation without sacrificing throughput and cell viability.

1.2 Dielectrophoresis

The ease of integrating a nonuniform electric field of a favorable scaling into microfluidic systems creates opportunities for exploiting dielectrophoresis to trap, separate, and manipulate microparticles. The DEP force arises from the induced dipole moment on the particles suspended in a medium with a different dielectric permittivity when exposed to a nonuniform electric field.⁶² In an isotropic medium of permittivity ϵ_m , the time-averaged DEP force, $\langle F_{DEP} \rangle$, exerted by a homogenous spherical particle with a radius a in an electric field E can be described by

$$\langle F_{DEP} \rangle = 2\pi\epsilon_m a^3 \operatorname{Re}[\kappa_{CM}(\omega)] \nabla |E_{RMS}|^2, \quad (1.1)$$

where the $\kappa_{CM}(\omega)$ is the complex Clausius-Mossotti (CM) factor, and can be written in terms of the complex permittivity of the particle ($\tilde{\epsilon}_p$) and surrounding medium ($\tilde{\epsilon}_m$)

$$\kappa_{CM} = \frac{\tilde{\epsilon}_p - \tilde{\epsilon}_m}{\tilde{\epsilon}_p + 2\tilde{\epsilon}_m}. \quad (1.2)$$

The complex permittivity:

$$\tilde{\epsilon} = \epsilon - i\frac{\sigma}{\omega}, \quad (1.3)$$

in which ϵ and σ are respectively the electric permittivity and conductivity, $i = \sqrt{-1}$, and ω is the frequency (in radians) of the electric field. A more in depth discussion of DEP occurs in chapter 2.

The DEP force is dependent on the difference between the dielectric properties of the particle and the surrounding media (κ_{CM}) and the field gradient ($\nabla |E|^2$). The former indicates that DEP can be a promising tool to probe the intrinsic electric properties of cells. The latter is also particularly interesting because the amplitude square dependence suggests that the sorting sensitivity of DEP-based cell separation can be improved by increasing the field gradient. Furthermore, the DEP force is independent of the field polarity.

In recent decades, DEP based cell isolation has been extensively investigated. One of the challenges is to increase the local electric field gradient without inducing strong joule heating. This is mainly achieved by designing embedded electrodes or controlling insulator channel

geometries. Various DEP electrodes, such as planar metallic and indium tin oxide (ITO) thin film electrodes,^{18, 79} liquid electrodes,¹³ 3D conductive PDMS electrodes,^{53, 52, 54} and metal alloy microspheres,⁵⁵ have been reported for multipurpose cell analysis. For instance, utilizing DEP and microfluidics, the metastatic human breast cell line MDA231 were differentiated from diluted blood by selective trapping of cancer cells onto microelectrodes while blood cells were swept downstream.⁶ DEP capture of individual cells can be achieved with addressable electrodes for real-time monitoring of cell functional processes, for example, to monitor the dynamic functional responses of calcein-labeled HL-60 cells to stimuli,⁷⁶ and can be released for further investigation. Particle separation based on size was achieved using conducting sidewall PDMS electrodes.⁵⁴ On the other hand, insulator based DEP (iDEP) commonly involves insulating posts,^{20, 49, 50} hurdles,^{47, 46, 45, 35}, constrictions,^{19, 83, 10} curvatures,^{84, 81, 82} and oil obstacles^{74, 3} that cause a spatial varying electric field, generating the DEP force. Compared to electrode-based DEP, iDEP offers multiple advantages, such as reduced joule heating and fouling issues while eliminating complex electrode fabrication. For example, live and dead human leukemia cells can be isolated utilizing contactless DEP under AC electric fields.⁷⁰ DC selective trapping of gram positive and gram negative bacteria can be achieved using a channel with an array of insulating posts.⁵¹ Recently, by integrating three dimensional insulating microstructures into DEP based microfluidic systems (3DiDEP), for example utilizing a 3D insulating curved ridge,³⁵ continuous particle separation with high sensitivity and throughput has been realized. Additionally, successful implementation of 3DiDEP for discriminating bacteria by selective immobilization based on cell surface polarizabilities at the strain level has been reported by Braff et al.,^{11, 12} suggesting that 3DiDEP can be a promising technique for strain level cell separation. The key advantage of 3DiDEP is that, with the same voltage applied, one can create a local electric field gradient in 3DiDEP systems an order of magnitude higher than in the two dimensional iDEP systems, and thus achieve much higher separation sensitivity.

1.3 Cell phenotype screening

In order to keep pace with the increasing exploration of microbe phenotypes for various applications, such as environmental bioremediation, energy harvesting, bacterial transformation, and clinical diagnosis, high-sensitive phenotyping techniques must be developed. We hypothesize that a variety of cell phenotypes can be associated with cell surface polarizabilities. The high sorting sensitivity enables 3DiDEP to be a promising technique to measure cell envelope

polarizabilities, and thus to identify changes in cell surface phenotypes. The absence and increasing need for such a phenotyping method with high throughput and sensitivity motivates this work. Ultimately, the objective of this work is to develop a microfluidic device for continuous cell separations based on cell envelope polarizability. As shown in **Figure 1-1**, the scenario is that a cell suspension with diverse surface polarizabilities can be separated into several different outlet streams continuously with high throughput. This technique can be used as fast phenotyping steps before and after various biochemical studies for efficiency assessment, and for selecting candidate microbes of interest from a heterogeneous cell population.

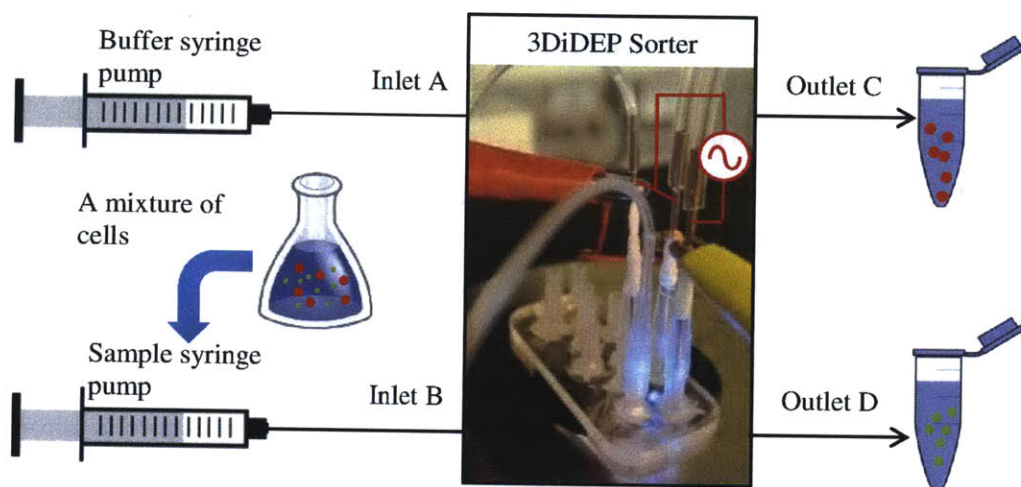


Figure 1-1 Overview of continuous cell separation using 3DiDEP

1.4 Organization

In this work, a 3DiDEP microdevice was developed for continuous particle separation based on polarizability. The underlying physics of dielectrophoresis, and the requirements of electrical relaxation time scales to focus on cell surface analysis is discussed in chapter 2. In chapter 3, the design of the microchannel geometry and the microfabrication process are illustrated. The governing principles to manipulate particle motions in 3DiDEP systems are discussed in chapter 4. In addition, the impact of insulating channel geometries on separation sensitivity will be elucidated using models of electric and hydraulic resistances. Numerical modeling for prediction of particle trajectories and electrothermal flow analysis are included in chapter 4. The evaluation of the performance of the 3DiDEP device was conducted by running experiments with

polystyrene beads with different diameters. Experimental observation and conclusions with discussion of potential future work are provided in chapters 5 and 6.

Chapter 2

Principles of Dielectrophoresis

2.1 Introduction

As discussed in the preceding section, compared to existing cell separation methods, dielectrophoresis is a more versatile technique that can distinguish cells not only based on their size and density, but also on their dielectric properties. This unique advantage of DEP opens the possibility of cell characterization at a more sensitive level, and thus enables more accurate biochemical study. Unlike linear electrokinetic phenomena, DEP is not dependent to the net charge of the particle and the electric field polarity. We now elaborate the principles of DEP in depth. The governing equations illustrated in this section will be used in the numerical modeling and experimental discussion in the following sections.

2.2 Field induced dielectric polarization and DEP

We first examine the response of a spherical dielectric particle with a radius, a , suspended in a dielectric medium exposed to an AC electric field E . The external electric field gives rise to a net dipole moment, p , of the particle. In 2D spherical coordinates (r, θ) , the electric potential distributions inside the particle (φ_p) and in the medium (φ_m) can be obtained by solving the Laplace equation, $\nabla^2\varphi=0$, using the expansion in spherical harmonics with the following boundary conditions^{41, 33}

$$\varphi_p(r=a) = \varphi_m(r=a), \quad (2.1)$$

$$\tilde{\epsilon}_p (\nabla\varphi_p \cdot \mathbf{n})_{r=a} - \tilde{\epsilon}_m (\nabla\varphi_m \cdot \mathbf{n})_{r=a} = 0. \quad (2.2)$$

where \mathbf{n} is the normal vector of the particle-medium interface, and $\tilde{\epsilon}$ is the complex permittivity defined by Eqn. (1.3). The subscripts p and m denote the particle and medium phases, respectively. Assuming an external electric field parallel to the z axis far away from the particle, a far-field boundary condition can be expressed as

$$\varphi_m(r \rightarrow \infty) = -Ez = -Er \cos \theta. \quad (2.3)$$

Hence, the solutions can be obtained in the following form

$$\varphi_p = \sum_{n=0}^{\infty} A_n r^n P_n(\cos \theta), \quad (2.4)$$

$$\varphi_m = \sum_{n=0}^{\infty} \left[B_n r^n + \frac{C_n}{r^{(n+1)}} \right] P_n(\cos \theta). \quad (2.5)$$

where P_n is the n^{th} Legendre polynomial^{1,41}. Applying the boundary conditions given by Eqn. (2.1) and (2.3), only the case of $n = 1$ remains, i.e. $B_1 = -E$, and

$$A_n = B_n + \frac{C_n}{a^{2n+1}} \text{ for all } n, \quad (2.6)$$

Substituting the boundary condition given by Eqn. (2.2), we obtain

$$\frac{n\tilde{\epsilon}_p A_n}{\tilde{\epsilon}_m} = nB_n - (n+1) \frac{C_n}{a^{2n+1}} \text{ for all } n. \quad (2.7)$$

Hence, the potential distributions in the particle and medium phases are

$$\varphi_p = - \left(\frac{3\tilde{\epsilon}_m}{\tilde{\epsilon}_p + 2\tilde{\epsilon}_m} \right) Er \cos \theta, \quad (2.8)$$

$$\varphi_m = \left(\frac{\tilde{\epsilon}_p - \tilde{\epsilon}_m}{\tilde{\epsilon}_p + 2\tilde{\epsilon}_m} \right) \frac{Ea^3}{r^2} \cos \theta - Er \cos \theta. \quad (2.9)$$

respectively. Eqn. (2.9) indicates that the potential in the medium is a combination of the potential of the dipole moment and that of the external field. Recalling that the potential of a dipole with a dipole moment, \mathbf{p} , in free space is given by³³

$$\varphi = \frac{\mathbf{p} \cdot \mathbf{r}}{4\pi\epsilon_0 r^3} = \frac{p \cos \theta}{4\pi\epsilon_0 r^2}, \quad (2.10)$$

and comparing it with the first term in Eqn. (2.9), we can find the effective dipole moment of the spherical particle

$$\mathbf{p} = 4\pi\epsilon_m a^3 \left(\frac{\tilde{\epsilon}_p - \tilde{\epsilon}_m}{\tilde{\epsilon}_p + 2\tilde{\epsilon}_m} \right) \mathbf{E}, \quad (2.11)$$

which can also be expressed in terms of an effective polarizability¹⁶, $\tilde{\alpha} = 3\epsilon_m \kappa_{CM}$, as

$$\mathbf{p} = \tilde{\alpha} V \mathbf{E}, \quad (2.12)$$

where V denotes the volume of the particle and κ_{CM} is the Clausius-Mossotti factor defined in the preceding section. A net force, F_{DEP} , on this induced dipole is given by⁶⁸

$$\mathbf{F}_{DEP} = (\mathbf{p} \cdot \nabla) \mathbf{E}, \quad (2.13)$$

with the assumption that the dipole dimension is small compared with the characteristic length across which the nonuniform electric field acts⁵⁸. For DC electric field, the force can be directly obtained by substituting Eqn. (2.11) into (2.13), which gives

$$\mathbf{F}_{DEP} = 4\pi\epsilon_m a^3 \kappa_{CM} (\mathbf{E} \cdot \nabla) \mathbf{E} = 2\pi\epsilon_m a^3 \kappa_{CM} \nabla (\mathbf{E} \cdot \mathbf{E}). \quad (2.14)$$

In an AC electric field with a constant phase, the potential can be described in terms of the frequency, ω , as

$$\varphi(\mathbf{x}, t) = \text{Re}[\tilde{\varphi}(\mathbf{x}) \exp(i\omega t)], \quad (2.15)$$

where $\tilde{\varphi} = \varphi_r + i\varphi_i$ is the complex potential, \mathbf{x} denotes the spatial vector, and t is the time. The time-averaged DEP force, $\langle \mathbf{F}_{DEP} \rangle$, is then derived by taking the average over a period of the AC forcing, T , of the harmonic function in Eqn. (2.13), giving¹⁶

$$\langle \mathbf{F}_{DEP} \rangle = \frac{1}{T} \int_0^T (\tilde{\mathbf{p}} \cdot \nabla) \tilde{\mathbf{E}} dt = \frac{1}{2} \text{Re}[(\tilde{\mathbf{p}} \cdot \nabla) \tilde{\mathbf{E}}^*], \quad (2.16)$$

where the asterisk denotes the complex conjugate. From Eqn. (2.12), the effective particle dipole moment is then given by

$$\tilde{\mathbf{p}} = \tilde{\alpha} V \mathbf{E} \exp(i\omega t). \quad (2.17)$$

Assuming a constant phase of the electric field, here the field, \mathbf{E} , is considered to be real. Combining Eqn. (2.16) and (2.17) gives the same expression to Eqn. (1.1)

$$\langle F_{DEP} \rangle = \frac{V}{4} \text{Re}[\tilde{\alpha}] \nabla(\mathbf{E} \cdot \mathbf{E}) = \pi \varepsilon_m a^3 \text{Re}[\kappa_{CM}] \nabla |E|^2. \quad (2.18)$$

The κ_{CM} and hence the time-averaged DEP force in Eqn. (2.18) is frequency dependent. At low frequencies $\omega \rightarrow 0$, κ_{CM} only depends on the relative values of σ_p and σ_m

$$\kappa_{CM} \rightarrow \frac{\sigma_p - \sigma_m}{\sigma_p + 2\sigma_m}. \quad (2.19)$$

On the other hand, at high frequencies $\omega \rightarrow \infty$,

$$\kappa_{CM} \rightarrow \frac{\varepsilon_p - \varepsilon_m}{\varepsilon_p + 2\varepsilon_m}. \quad (2.20)$$

We observe from Eqn. (2.18)-(2.20) that the general DEP behavior of the particle is dependent on the real part of κ_{CM} , and thus the relative values of conductivity and permittivity between the particle and the medium. When $\text{Re}[\kappa_{CM}] > 0$, particles are attracted to the high electric field region in what is known as positive DEP; at $\text{Re}[\kappa_{CM}] < 0$, particles are repelled away from the high electric field region, and this is known as negative DEP.

2.3 Scaling of the relaxation time

By setting the real part of κ_{CM} to be zero, we can obtain the crossover frequency (in hertz), ω_c , wherein the DEP force changes direction.

$$\omega_c = \frac{1}{2\pi} \sqrt{\frac{(\sigma_m - \sigma_p)(\sigma_p + 2\sigma_m)}{(\varepsilon_p - \varepsilon_m)(\varepsilon_p + 2\varepsilon_m)}}. \quad (2.21)$$

At first glance, for latex particles that with permittivity and conductivity typically lower than those of the liquid medium, the ω_c does not exist and the $\text{Re}[\kappa_{CM}]$ is always negative. However, this prediction is inconsistent with the experimental observation of positive DEP of latex particles at low frequencies by various works^{29, 30, 75}. Actually for the cases where there is no surface charge and electrical double layer, the well-known Maxwell-Wagner Theory^{56, 77} is particularly valid, and thus the prediction of ω_c based on the dielectric properties of the particle and medium is accurate. Nevertheless, it should be noted that this theory implies a model assuming a parallel

RC circuit (R being the resistance and C the capacitance) on both sides of the interface. Thus, the polarization is assumed due to dielectric polarization at high applied frequencies but by conduction of free charges at low frequencies. This theory does not account for the polarization that results from the conductivity gradient near the interface, which often involves extended polarized layers and diffuse layers. For most circumstances of latex particles and bioparticles, the nonlinear extended polarized and diffuse layers should not be neglected. Therefore, several modifications to the classical theory are necessary to capture the omitted effects of diffusive and tangential ion fluxes at the interface. To account for the effect of the conducting Stern layer and collapsed diffuse double layer in the thin diffuse layer and small zeta potential limit, it was first proposed by O’Konski⁶⁰ (1960) to modify the particle conductivity, giving an effective complex particle permittivity of the form

$$\tilde{\epsilon}_p = \epsilon_p - \frac{i}{\omega} (\sigma_p + A\sigma_m). \quad (2.22)$$

The additional term arises because of the Stern layer conductance and the diffuse layer, resulting in a higher effective conductivity of the particle than that of the medium. Hence, for the conditions that the pure particle conductivity and permittivity are negligible, the crossover frequency (in hertz) can be modified as

$$\omega_c = \frac{1}{2\pi} \sqrt{\frac{(A-1)(A+2)}{2}} \frac{\sigma_m}{\epsilon_m}. \quad (2.23)$$

Not surprisingly, the O’Konski model is invalid under many circumstances because it does not capture the effects of diffuse layer capacitive charging, Stern layer adsorption, and diffusive relaxation in the tangential direction. However, for the cases of thin diffuse layer where tangential conductive charging in the diffuse layer is negligible, the O’Konski model is still suitable.

Based on simple scaling theory, there are several different relaxation time scales and crossover frequency behaviors³². With the limit of low medium conductivity and a diffuse layer thickness much larger than the particle size, normal conduction is prominent. Thus, the crossover frequency for nonconducting particles is⁸⁰

$$\omega_c \sim \frac{D}{\lambda_D^2}, \quad (2.24)$$

where D is the diffusion coefficient in the medium, and λ_D is the diffuse layer thickness. For a higher medium conductivity corresponding to $\lambda_D \sim a$, the diffuse layer allows both tangential conduction and normal capacitive charging, giving^{26,4}

$$\omega_c \sim \frac{D}{\lambda_D a}. \quad (2.25)$$

For a very high medium conductivity, the double layer is increasingly screened, corresponding to a relaxation into a tangential Poisson-Boltzmann equilibrium. The diffuse layer thickness is much smaller than the particle size, and the crossover frequency becomes^{59,31}

$$\omega_c \sim \frac{D}{a^2}. \quad (2.26)$$

Between the two crossover frequencies described by Eqn. (2.25) and (2.26), there is an intermediate region where the Poisson-Boltzmann equilibrium is not valid. A different polarization mechanism due to current penetration to the particle surface should be invoked⁵. With the relatively high medium conductivity, the normal conductive charging occurs at only one pole of the particle instead of everywhere due to the screening effect of the thin diffuse layer at the pole. The normal polar charging then drives tangential ion transport that leads to double layer polarization. The relaxation time of the induced particle dipole is then determined by the balance between the polar charging flux and the tangential conduction flux, giving a field-dependent crossover frequency⁵

$$\omega_c \sim \left(\frac{D}{a^2} \right) \left(\frac{E_s \lambda_D F}{RT} \right)^2, \quad (2.27)$$

where E_s denotes the surface electric field.

2.4 Dielectric cell model

The κ_{CM} derived in section 2.2 is only valid for spherical particles, and thus not suitable for most bacteria and cells. Saville *et al.* generalized the result of κ_{CM} to that of a prolate spheroid⁶⁶. The volume of the particle, V , is replaced by the spheroid volume $V = 4\pi a^2 b/3$, where a and b are the

lengths of the short and long semiaxes of the spheroid, respectively. The Clausius-Mossotti factor is then replaced with^{38, 66}

$$\kappa_{CM}(\omega)_{//,\perp} = \frac{1}{3} \left[\frac{\tilde{\epsilon}_p - \tilde{\epsilon}_m}{\tilde{\epsilon}_m + L_{//,\perp}(\tilde{\epsilon}_p - \tilde{\epsilon}_m)} \right], \quad (2.28)$$

along ($//$) and perpendicular (\perp) to the external electric field. L is the depolarizing factor that can be expressed as

$$L_{//} = 1 - 2L_{\perp} = (\sinh \xi)^2 Q, \quad (2.29)$$

where

$$Q(z) = \frac{z}{2} \ln \left(\frac{z+1}{z-1} \right) - 1. \quad (2.30)$$

The constant, ξ , is defined such that $\tanh \xi = a/b$, and $z = \cosh \xi$. It's clear that for a spherical particle, $a=b$, $n=1/3$, and hence the κ_{CM} derived in section 2.2 is recovered. With the elongated semiaxis and large aspect ratio of the prolate spheroid, κ_{CM} can be significantly increased compared with that of a spherical particle.

Another reason that the model in section 2.2 is unsuitable for real cells is the omission of the anisotropic distribution of cell dielectric properties. One of the first models that demonstrate the dielectric properties of a cell was proposed by Hoerber and Hochmuth in 1970³⁷. They described a red blood cell as a sphere of highly conducting cytoplasm surrounded by an insulating membrane. Generalizing the single cell model to a multi-shelled model where a highly conducting sphere is enclosed by several concentric less conducting shells has proven reliable for the analysis of synaptosomes⁴⁰ and yeast cells³⁹. For some non-spherical cells, e.g. *Escherichia coli*, a more accurate model is required. Castellarnau *et al.* developed a two-shell prolate ellipsoid model¹⁵ (**Figure 2-1 a**) to analyze the dielectric parameters of *E. coli*, including the complex permittivity of the cytoplasm ($\tilde{\epsilon}_{cyto}$), the cytoplasmic membrane ($\tilde{\epsilon}_{mem}$), and the cell wall ($\tilde{\epsilon}_{wall}$). Given the relationship of each neighboring layers, the factor κ_{CM} is calculated in three steps. First, the effective dipole factor of the two inner layers, X_I , can be defined through Eqn. (2.28-2.30), where the complex permittivity of the particle ($\tilde{\epsilon}_p$) and medium ($\tilde{\epsilon}_m$) are replaced with that of the

cytoplasm ($\tilde{\epsilon}_{cyto}$) and membrane ($\tilde{\epsilon}_{mem}$), respectively. Then the impact of outer layer is considered by defining the effective dipole factor of the whole particle as

$$X_{2,i} = \frac{1}{3} \left[\frac{(\tilde{\epsilon}_{mem} - \tilde{\epsilon}_{wall}) + 3X_{1,i}\rho_1[\tilde{\epsilon}_{mem} + L_{2,i}(\tilde{\epsilon}_{wall} - \tilde{\epsilon}_{mem})]}{[\tilde{\epsilon}_{wall} + L_{2,i}(\tilde{\epsilon}_{mem} - \tilde{\epsilon}_{wall})] + 3X_{1,i}\rho_1 L_{2,i}(1 - L_{2,i})(\tilde{\epsilon}_{mem} - \tilde{\epsilon}_{wall})} \right], \quad (2.31)$$

where $i=x,y,z$ are the three axes of the ellipsoid. In addition, $L_{2,i}$ is defined in Eqn. (2.29) and (2.30), where the factor, ξ_2 , is redefined by $\tanh \xi_2 = (a + d_{mem})/(b + d_{mem})$. The volume ratio, ρ_1 , is given by

$$\rho_1 = \frac{a^2 b}{(a + d_{mem})^2 (b + d_{mem})}. \quad (2.32)$$

Similarly, the total Clausius-Mossotti factor can then be expressed by considering the effect of the surrounding medium as

$$K_i(\omega) = \frac{1}{3} \left[\frac{(\tilde{\epsilon}_{wall} - \tilde{\epsilon}_m) + 3X_{2,i}\rho_2[\tilde{\epsilon}_{wall} + L_{3,i}(\tilde{\epsilon}_m - \tilde{\epsilon}_{wall})]}{[\tilde{\epsilon}_m + L_{3,i}(\tilde{\epsilon}_{wall} - \tilde{\epsilon}_m)] + 3X_{2,i}\rho_2 L_{3,i}(1 - L_{3,i})(\tilde{\epsilon}_{wall} - \tilde{\epsilon}_m)} \right]. \quad (2.33)$$

With the same assumptions above, the factor, ξ_3 , is redefined by

$$\tanh \xi_3 = \frac{a + d_{mem} + d_{wall}}{b + d_{mem} + d_{wall}}, \quad (2.34)$$

and the volume ratio is given by

$$\rho_2 = \frac{(a + d_{mem})^2 (b + d_{mem})}{(a + d_{mem} + d_{wall})^2 (b + d_{mem} + d_{wall})}. \quad (2.35)$$

Finally, the DEP behavior of the cell can be evaluated by taking the average of the real part of the Clausius-Mossotti factor in the three axes of polarization:

$$\kappa_{CM} = \frac{1}{3} \sum_{i=x,y,z} \text{Re}[K_i(\omega)]. \quad (2.36)$$

The preceding derivation of the multi-shell cell model has proven useful for ellipsoidal cells. In the case of polystyrene beads, the homogeneous spherical particle model (**Figure 2-1 b**) based on

O’Konski theory can be used. The factor κ_{CM} can be evaluated by Eqn. (1.2) and (1.3), but the conductivity of particle is modified by⁷³

$$\sigma_p = \sigma_s + \frac{2K_s}{a}, \quad (2.37)$$

where σ_s is the intrinsic conductivity of the solid particle. Generally, the intrinsic conductivity is negligible for polystyrene beads, and thus the effective conductivity of the particle is dominated by the surface conductance (K_s) and particle radius (a).

To predict the DEP behavior of particles and cells in this study, and to determine the frequency regime where cell surface properties dominate the DEP responses, the Clausius-Mossotti factor of *E. coli* strain 5K and polystyrene beads with different diameters (1 μm and 6 μm) is calculated based on the models. The dielectric and particle geometrical parameters are summarized in the Table 2.1. **Figure 2-1 (c and d)** shows the variation of the real part of κ_{CM} with respect to the frequency of the applied electric field in different suspending medium conditions. It also indicates that an upper frequency threshold, i.e., the first crossover frequency, can be found in the 100 kHz ~ 1 MHz frequency range for *E. coli* 5K, and 20 kHz ~ 200 kHz frequency range for polystyrene beads, for certain medium conductivities. Below these frequency thresholds, the main contributions to DEP response of the particles and cells are due to the dielectric properties of the outermost layer. Therefore, in order to separate particles and cells based on their envelope properties, the applied frequencies should not exceed the upper frequency limitation determined by the relaxation time of the outermost layer. The required frequency limitations of the applied field will be further discussed in Chapter 4.

Table 2.1 Parameters for the calculation of Clausius-Mossotti factor

Particles	Conductivity (S/m); Surface conductance (nS)	Relative permittivity	Size (μm)
<i>E. coli</i> 5K ¹⁵	$\sigma_{cyto}=0.48$; $\sigma_{mem}=2.59 \times 10^{-8}$; $\sigma_{wall}=0.058$.	$\epsilon_{cyto}=49.8$; $\epsilon_{mem}=9.8$; $\epsilon_{wall}=78$; $\epsilon_m=78.5$.	$a=0.75$; $b=1.5$; $d_{mem}=0.008$; $d_{wall}=0.05$.
Polystyrene beads ⁷³	$\sigma_s=0$; $K_s=1.2$	$\epsilon_p=2.55$; $\epsilon_m=78.5$.	$2a=1$ and 6

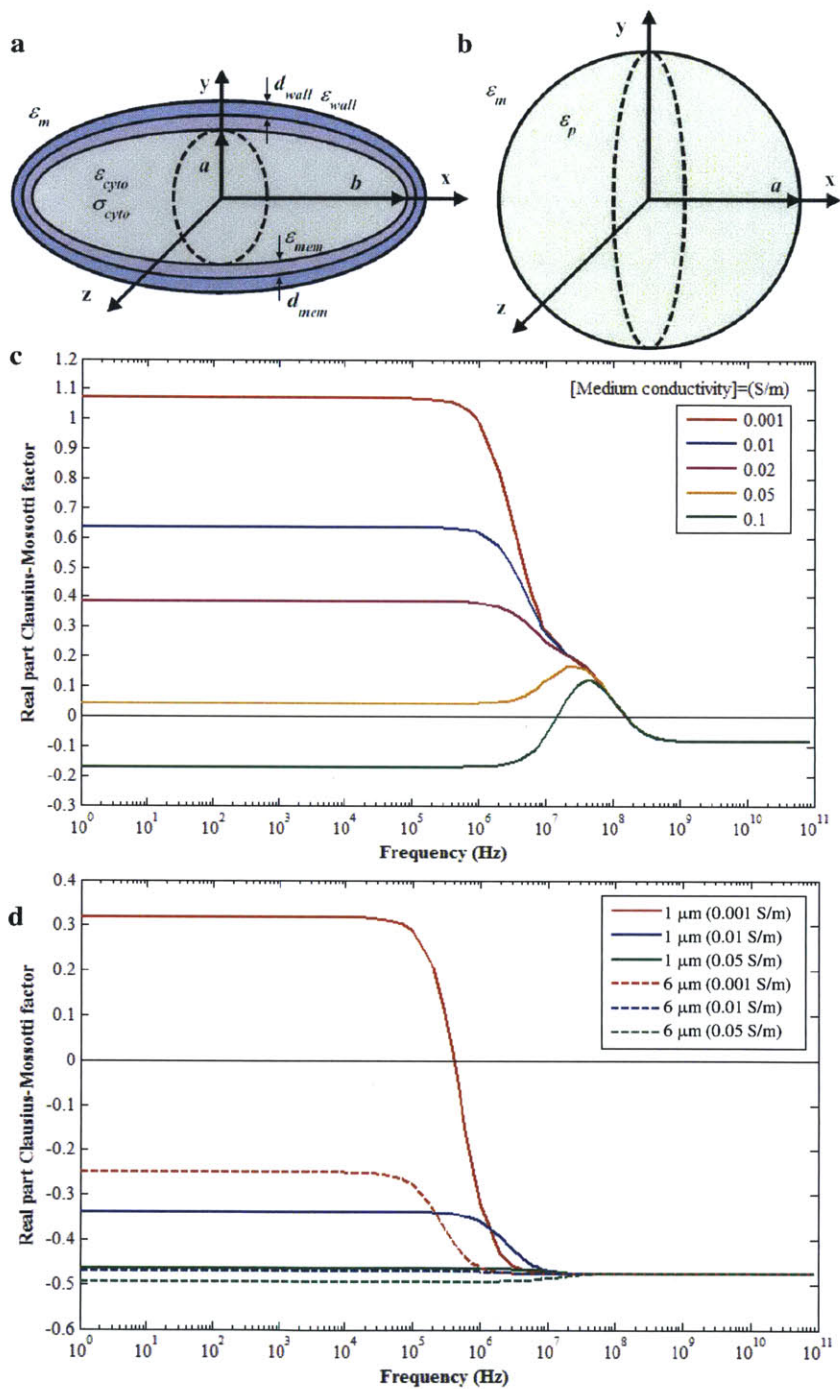


Figure 2-1 Diagrams of (a) the ellipsoid two-shell model considered for *E. coli* cells and (b) the homogeneous spherical model for polystyrene beads. Variation of the real part of Clausius-Mossotti factor of (c) *E. coli* 5K¹⁵ and (d) polystyrene beads⁷³ with changes in the medium conductivity (in S/m).

Chapter 3

3DiDEP Sorter Design and Fabrication

3.1 Introduction

Having demonstrated the underlying physics of DEP in chapter 2, it is clear that the separation sensitivity is significantly dependent on the electric field gradient. This implies that for iDEP systems, the constriction ratio between the cross-sectional areas of the open channel and that of the constriction is essential for increasing iDEP separation sensitivity. A detailed investigation of the influence of the insulating channel geometry on the distribution of electric field and flow field will be discussed in chapter 4. However, the channel constriction ratio should not be arbitrarily high, not only because of limitations of the intrinsic hydraulic resistance of the fluid, but also because of limitations of the fabrication procedures. In this chapter, we demonstrate the design of a 3DiDEP microdevice consisting a three dimensional constriction that can increase the constriction ratio by an order of magnitude compared to 2D cases. A micro milling technique was used to fabricate the 3DiDEP microchannels in Poly (methyl methacrylate) (PMMA) substrates.

3.2 Design of 3DiDEP channel geometry

We demonstrate a 3DiDEP microdevice designed for binary particle sorting. It consists of four channel branches connecting to four different fluid reservoirs, including two inlets and two outlets. As shown in **Figure 3-1c**, inlet A and inlet B are for introducing the buffer sheath flow and particle suspension, while outlet C and outlet D are for collecting the separated particles. The dimensions of the cross-sectional areas of each channel branch are $150 \times 150 \mu\text{m}^2$ for inlet A and outlet C, $150 \times 80 \mu\text{m}^2$ for inlet B, $600 \times 500 \mu\text{m}^2$ for outlet D, and $50 \times 80 \mu\text{m}^2$ for the constriction. More detailed information about the channel geometry can be found in **Appendix A**. For particle separation, the scenario is that with both inlet A and outlet C connected to the AC signal while outlet D is grounded, an electric field will be established in the y-direction. The constriction creates a high electric field gradient, and thus a strong DEP force, perpendicular to the main bulk flow direction (x-direction), which is the key factor influencing particle deflection in the vicinity of the constriction. The medium and the particle suspension are designed to be

pumped into inlet A and B with a specific volumetric flow rate ratio to confine the particle stream towards the constriction. The channel geometry is designed such that all particle path lines terminate in outlet D when no electric field is applied.

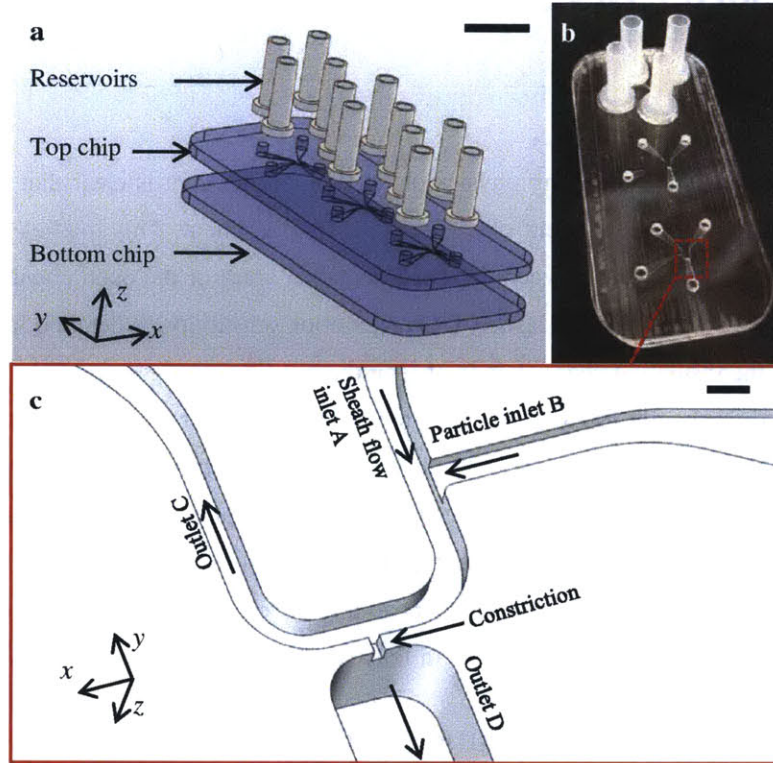


Figure 3-1 Design of the 3DiDEP microdevice. (a) Assembly process of the PMMA iDEP chip consisting of an array of three microchannels. (b) Completed 3DiDEP microdevice. (c) 3D CAD rendering of the machined PMMA surface with labeled channel branches. Scale bars: 1 cm (a), 200 μm (c).

3.3 Microfabrication of 3DiDEP devices

A variety of techniques exist for the fabrication of the microfluidic devices, including soft lithography⁷⁸, one of the most widely used methods, and micromachining^{67, 25}, embossing^{8, 7}, injection molding⁵⁷, as well as laser ablation^{48, 42, 71}. The most common procedure of soft lithography involves the fabrication of a silicon wafer coated with a photoresist that is patterned via exposure to ultraviolet (UV) light through a mask with desirable geometries. Then the microchannel patterns can be transferred to an elastomeric material, typically polydimethylsiloxane (PDMS), by replica molding. Enclosed microchannels can be achieved by bonding the PDMS replica to a variety of materials after exposure to oxygen plasma. Soft

lithography provides many advantages, such as low cost, high resolution of patterning, and reusability of the silicon master. However, it requires bench top processes in clean rooms. The need of complex multiple layer fabrication and alignment is impractical for three dimensional channel geometries^{2, 43}. Additionally, the deformability and relatively unstable surface charge characteristic of PDMS may result in undesirable electrokinetic background flow in 3DiDEP systems.

PMMA and a micro milling technique were chosen for the Microfabrication in this work. Compared with PDMS, PMMA is stiffer and can be machined for fast 3D prototyping. The nonuniform surface charge distribution can be eliminated quickly by dynamic surface modification which will be discussed in chapter 5. In addition, the low autofluorescence and transparency of PMMA is desirable for fluorescence visualization. The 3DiDEP devices are fabricated on $25 \times 55 \text{ mm}^2$ PMMA pieces cut from 1.5 mm thick PMMA sheets (McMaster Carr, Princeton, NJ) by laser cutting. The machining process is operated by a Microlution 363-S Precision-optimized 3-axis micro machining platform (Chicago, IL, USA) controlled by a written G-code. Mastercam CAD/CAM software (Tolland, CT) is used to define the tool path and generate the G-code. The G-code used to fabricate the 3DiDEP is included in **Appendix B**. Micro end mills (Performance Micro Tool, Janesville, WI) with two flutes and different diameters (50.8 μm , 101.6 μm , 380.7 μm and 1.59 mm) are utilized for fabrication of channels with different widths and holes for the fluid reservoirs. The PMMA workpiece was mounted onto a pallet that is clamped by a fixture of the machine using a Crystalbond 555 temporary adhesive (SPI Supplies, West Chester, PA). This adhesive can melt above 50 °C, but remain solid at ambient temperatures so that the PMMA can be mounted onto the pallet and then detached easily by controlling the temperature using a hot plate. In order to maintain a parallel machining surface, a facing process using the 1.59 mm OD end mill was added prior to the channel machining process. A laser touch-off procedure is utilized to measure the tool offset in order to prevent the tools from breaking. The work plane was defined by feeding a tool, with no tip (or the back of an end mill) slowly into contact with the PMMA machining surface. Then both the heights of that tool and the machining end mills are measured using the laser. The differences between the end mill height and the blank tool height are set to be the tool offsets. Calibrations of tool length measurements were conducted for the 50.8 μm and 101.6 μm end mills. Strip-type grooves were milled into the PMMA substrates with different depths ($z = 0$ and $z = -50 \mu\text{m}$). Then the PMMA was cut into thin pieces, and the depths of the grooves were observed from the cross-sectional plane under the microscope

(**Figure 3-2**). It is clear that although the laser measurements are successful with end mills with an OD wider than around 100 μm , it is not sensitive enough to detect the tip of 50 μm end mills, and tends to underestimate its tool length. Therefore, based on the calibration results, an additional 50 μm tool length offset was set for the 50 μm end mill and incorporated in the G-code. There is an array of three microchannels fabricated on one PMMA chip, and the whole machining process takes about 25 minutes.

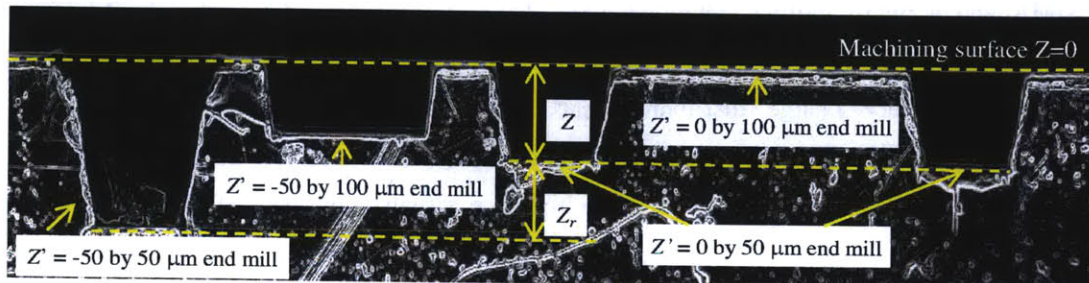


Figure 3-2 Tool length measurement calibration for 50 and 100 μm end mills. Cutting depths (Z') are set to be 0 μm and 50 μm to obtain a 50 μm reference distance (Z_r). The actual cutting depths (Z) were measured for the $Z'=0$ cases to determine the underestimation of tool length.

After micro milling, the PMMA chips were detached from the pallet by increasing the temperature using a hot plate. Then the machined chips were rinsed sequentially with acetone, methanol, isopropanol, and deionized water to clean the acrylic residues and coolant utilized during the milling process. In order to generate the enclosed microchannels, the machined PMMA chip is bonded to another blank chip cleaned with the same method following a solvent assisted thermal bonding process¹⁴. The bonding solvent consists of 47.5% dimethyl sulfoxide (DMSO), 47.5% deionized water, and 5% methanol. After applying about 50 μL of this bonding solvent in between the bonding surfaces of the machined and blank PMMA chips, the chips were compressed using an aluminum fixture and heated up by a furnace. The chips were heated up to 96 $^{\circ}\text{C}$ for 45 minutes, and then were cooled down with a constant rate towards 40 $^{\circ}\text{C}$ for another 45 minutes. An irreversible bond is achieved after the thermal bonding procedure with no noticeable PMMA deformation. Then the enclosed channels are flushed with deionized water to clean the remaining solvent. Fluid reservoirs are attached on top of the PMMA device using a Devcon five-minute epoxy purchased from McMaster Carr (Princeton, NJ). The assembly process is shown in **Figure 3-1a**, and the completed 3DiDEP microdevice is shown in **Figure 3-1b**.

Chapter 4

Analysis of 3DiDEP based particle separation

4.1 Introduction

In this chapter we will further investigate the physics that governs the motion of particles in 3DiDEP based separation systems. With low frequency AC electric fields, the particle mainly experiences two forces, namely the DEP force due to the nonuniform electric field and the Stokes' drag force due to the background flow field. The flow field may be caused by both the pressure difference across the channel and temperature gradients due to the electrothermal effects. The fluid field and the electric field are thus coupled mutually through two mechanisms, expressed by: the convective charge flux density term, $\nabla \cdot (\rho_e \mathbf{u})$, in the charge conservation equation, and the electrothermal body force in the Navier-Stokes equation. However, we aim to reduce the joule heating effect on 3DiDEP systems by properly designing the insulating geometry. By minimizing the temperature variation along the microchannel, the electrical and hydrodynamic effects can be decoupled. In this chapter, we will first study the governing equations with appropriate assumptions that may play significant roles in 3DiDEP systems. Then, serial electric resistance and parallel hydraulic resistance models are built to evaluate the effects of channel geometry on 3DiDEP separation sensitivity. Channel geometry factors and criteria for particle deflection are derived to optimize the channel design and experimental conditions. Ultimately, a decoupled numerical model is developed using COMSOL Multiphysics 4.4b (Burlington, MA, USA) to predict the distribution of the electric field, flow field, and particle trajectories. Since the temperature gradient within the microchannel may also influence the particle motion, a coupled electrothermal flow model is also established to evaluate the upper threshold for the applied electric field.

4.2 Governing equations and assumptions

4.2.1 Electric field

The electric conductivity of the PMMA is about 1×10^{-19} S/m, which is much smaller than that of the medium (500 μ S/cm) used for the particle suspension. With the assumptions of non-conducting PMMA, the electric field is confined within the fluid domain and governed by

$$\nabla \cdot (\epsilon_m \mathbf{E}) = \rho_e \quad (4.1)$$

$$\nabla \cdot (\sigma_m \mathbf{E} + \rho_e \mathbf{u}) + \frac{\partial \rho_e}{\partial t} = 0. \quad (4.2)$$

Gauss's law (Eqn. 4.1) and charge conservation (Eqn. 4.2) imply a quasi-static assumption where the electromagnetic wavelength is large compared with the characteristic length of the 3DiDEP system, and $\nabla \times \mathbf{E} = -\partial \mathbf{B} / \partial t = 0$ ³⁴. The bolded variables denote vector variables, and ρ_e is the volumetric free charge density. We assume that the charge rearrangement due to fluid flow ($\rho_e \mathbf{u}$) is much slower than that of the ohmic current ($\sigma_m \mathbf{E}$) and thus can be safely neglected⁶⁴. Additionally, since the fluid is neutral, a zero net volumetric charge density is assumed. Combining Eqn. (4.1) and (4.2) and assuming a sinusoidal applied electric field gives the expression for the electric potential,

$$\nabla \cdot [(\sigma_m + i\omega\epsilon_m)\nabla\phi] = 0. \quad (4.3)$$

For DC fields and AC fields with frequencies $f \leq \sigma_m / 2\pi\epsilon_m$ (on the order of 10 MHz), Eqn. (4.3) reduces to

$$\nabla \cdot (\sigma_m \nabla\phi) = 0. \quad (4.4)$$

4.2.2 Flow field

Assuming steady-state creeping flow, the flow field is governed by the Navier-Stokes equation and the continuity equation

$$0 = -\nabla p + \nabla \cdot (\eta \nabla \mathbf{u}) + \langle \mathbf{f}_e \rangle \quad (4.5)$$

$$\nabla \cdot \mathbf{u} = 0, \quad (4.6)$$

where p is the pressure, η is the dynamic viscosity of the fluid, and $\langle f_e \rangle$ is the time-averaged external body force due to electrothermal effects. The electrothermal force can be expressed by⁷²

$$\langle f_e \rangle = \langle \nabla \cdot (\varepsilon_m \mathbf{E}) \mathbf{E} - 0.5 (\mathbf{E} \cdot \mathbf{E}) \nabla \varepsilon_m \rangle, \quad (4.7)$$

where the first and second term on the right hand side are the Coulombic forces on free and bound charges, respectively. The gradient of the fluid permittivity, $\nabla \varepsilon_m$, is attributed to the temperature gradient, ∇T , caused by joule heating effects. The temperature dependence of the fluid properties including permittivity, conductivity and viscosity can be approximated by⁷²

$$\varepsilon_m(T) = \varepsilon_0 [1 + \alpha_T (T - T_0)] \quad (4.8)$$

$$\sigma_m(T) = \sigma_0 [1 + \beta_T (T - T_0)] \quad (4.9)$$

$$\eta(T) = 2.761 \times 10^{-6} \exp(1713/T), \quad (4.10)$$

where T_0 is the reference ambient temperature, and σ_0 is the medium electric conductivity corresponding to T_0 .

4.2.3 Temperature field

The electric field in the microchannel generates joule heating in the electrolyte, which is higher near the insulating constriction than the open areas due to the amplified local electric field. The heat generation results in a temperature gradient, which leads to convection in the fluid and diffusion through the PMMA substrates and ultimately into the surrounding air. The steady-state temperature distribution over the entire fluid domain is governed by

$$\rho C_p (\mathbf{u} \cdot \nabla T) = \nabla \cdot (k \nabla T) + \sigma_m \langle \mathbf{E} \cdot \mathbf{E} \rangle, \quad (4.11)$$

where ρ is the fluid density, C_p and k are the specific heat capacity and thermal conductivity of the fluid, respectively. The last term on the right hand side of Eqn. (4.11) is the time averaged joule heating.

4.2.4 Particle motion near the constriction

Low frequency AC electric fields applied so we assume that electroosmosis of the bulk flow and the electrophoresis are negligible. An additional assumption is that the particle-particle interaction can be neglected given the low particle suspension density ($\sim 1 \times 10^6$ particles per mL). With the background flow condition that all streams originating from the particle inlet (white in **Figure 4-1**) terminate at the lower outlet (Outlet D), all particles moving in the 3DiDEP channel should be confined towards the constriction following the streamlines when no electric field is applied. Upon application of the electric field, particles experience two main forces, namely the negative DEP force (F_{DEP}) that repels them away from the constriction and the Stokes' drag force due to the background fluid flow (F_D) that drives them through the constriction. In the vicinity of the constriction, more polarizable particles (red in **Figure 4-1**) experience F_{DEP} higher than F_D , being deflected towards the upper streams. In contrast, F_D dominates the motion of less polarizable particles (green), still driving them towards Outlet D.

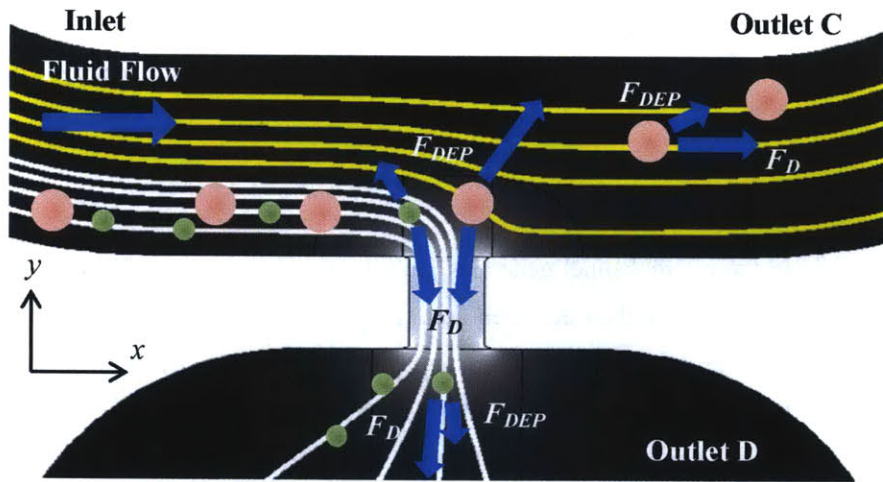


Figure 4-1 Schematic of forces experienced by particles in the vicinity of the constriction. Also illustrated are the y-component of $\nabla|E^2|$ (background grayscale, lighter region indicates higher values) and streamlines originating from the particle inlet (white) and the sheath flow inlet (yellow). More polarizable particles (red) near the constriction experience a dielectrophoretic force (F_{DEP}) that can exceed the drag force (F_D) due to the background flow field, being deflected towards the upper streams, while the opposite is true for less polarizable particles (green).

4.3 Channel geometry factor χ

In iDEP systems, the electric field distribution is controlled by designing the geometry of the insulating channels. Sharp variations in channel cross-sectional areas with respect to the flow direction can significantly increase the gradient of the electric field and therefore the sensitivity of 3DiDEP particle sorting. On the other hand, fluid flow in the microchannels is also affected by the channel geometry. Due to mass conservation, reduced channel cross-sectional area decreases the time for the DEP force to act on particles, and thus limits the sorting sensitivity. The ideal condition is that the time scales of the DEP lateral migration across streamlines and hydrodynamic longitudinal displacement are of the same order. In addition, the minimization of steric effects should also be considered for microchannel design. In this section, we will first extract some key channel geometry factors, and discuss their impact on both electric and flow fields. Then, we will conclude with a criterion for particle separation to guide channel design.

4.3.1 Serial electric resistor model

For a simple straight channel with a constriction, the local electric field near the constriction region is proportional to the ratio between the cross-sectional areas of the main channel and the constriction (constriction ratio)^{11, 12}. However, the 3DiDEP sorter consists of multiple branches with various channel widths and depths. Therefore, both of the constriction ratios with respect to the cross-sectional areas of the inlet and outlet channels play a role in the electric field distribution. We demonstrate an effective constriction ratio, χ , in terms of the cross-sectional area ratio between channel 1 and the constriction ($\chi_1 = A_1/A_0$) as well as the ratio between channel 2 and the constriction ($\chi_2 = A_2/A_0$) (Figure 4-2). Given the symmetry of the 3DiDEP channel, we imagine the left half of the channel as resistors in a series, with resistances in terms of their corresponding channel cross-sectional area ratios:

$$R_1 = \frac{R_0}{2\chi_1} \frac{L_1}{L_0}, \quad (4.1)$$

$$R_2 = \frac{R_0}{\chi_2} \frac{L_2}{L_0}, \quad (4.2)$$

where R and L denote the electric resistance and length of the corresponding channel sections, while the subscripts, 1, 0, and 2, represent channel 1, the constriction, and channel 2, respectively (Figure 4-2).

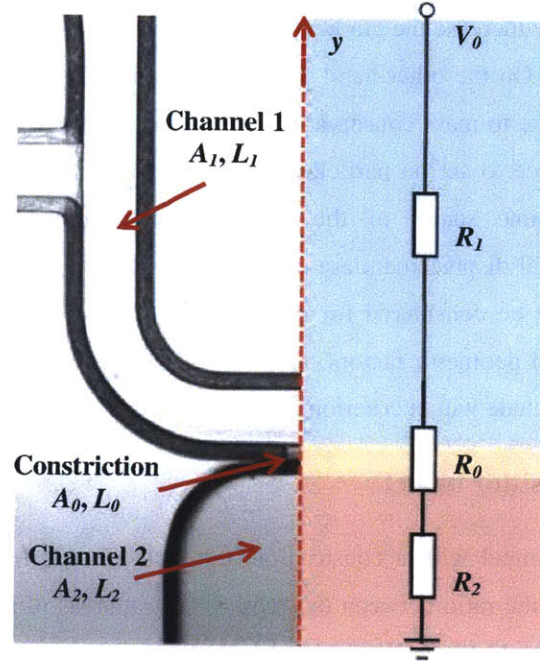


Figure 4-2 Schematic for the serial electric resistor model to evaluate the impact of the insulating channel geometry on the electric field distribution. A , L and R are the cross-sectional area, length, and corresponding resistance of the channel sections. The subscripts, 1, 0, and 2, denote channel 1, the constriction, and channel 2, respectively.

Then, with the Ohm's law, the total current and local electric field near the constriction region can be expressed by

$$I = \frac{V_0}{R_0} \left(\frac{1}{\frac{1}{2\chi_1} \frac{L_1}{L_0} + 1 + \frac{1}{\chi_2} \frac{L_2}{L_0}} \right) = \sigma E A_0, \quad (4.3)$$

where V_0 is the RMS voltage difference applied across the channel. The electric field near the constriction region, E , can be further simplified as

$$E = \frac{V_0}{L} \chi, \text{ where } \chi = \left(\frac{1}{\frac{\alpha_1}{2\chi_1} + \alpha_0 + \frac{\alpha_2}{\chi_2}} \right). \quad (4.4)$$

L is the total length of the channel, and the dimensionless parameter, α , is the ratio between lengths of the corresponding channel section and the whole channel ($\sum_{i=0.1.2} \alpha_i = 1$). Thus, the y

component of the electric field squared at the constriction, $\nabla_y |E^2|$, can be approximated as

$$\nabla_y |E^2| \cong \frac{1}{w} \left(\frac{V_0}{L} \right)^2 \chi^2, \quad (4.5)$$

where w is the characteristic length scale for the lateral DEP migration across the streamlines. For the 3DiDEP channel, w scales to the width of the constriction, $w_0=50 \mu\text{m}$. In order to verify the relationship between $\nabla_y |E^2|$ and χ as demonstrated in Eqn. (4.5), the average $\nabla_y |E^2|$ over the cross-sectional plane of the constriction (illustrated in red in upper left inset of **Figure 4-3**) was evaluated using COMSOL Multiphysics 4.4b software with various values of χ . The channel length parameters are chosen to be $\alpha_0 = 0.05$, $\alpha_1 = 0.41$, $\alpha_2 = 0.54$, respectively. **Figure 4-3** indicates a consistent result that $\nabla_y |E^2|$ is proportional to the effective constriction ratio squared

($\nabla_y |E^2|$ is normalized by $\frac{V_0^2}{L^3}$).

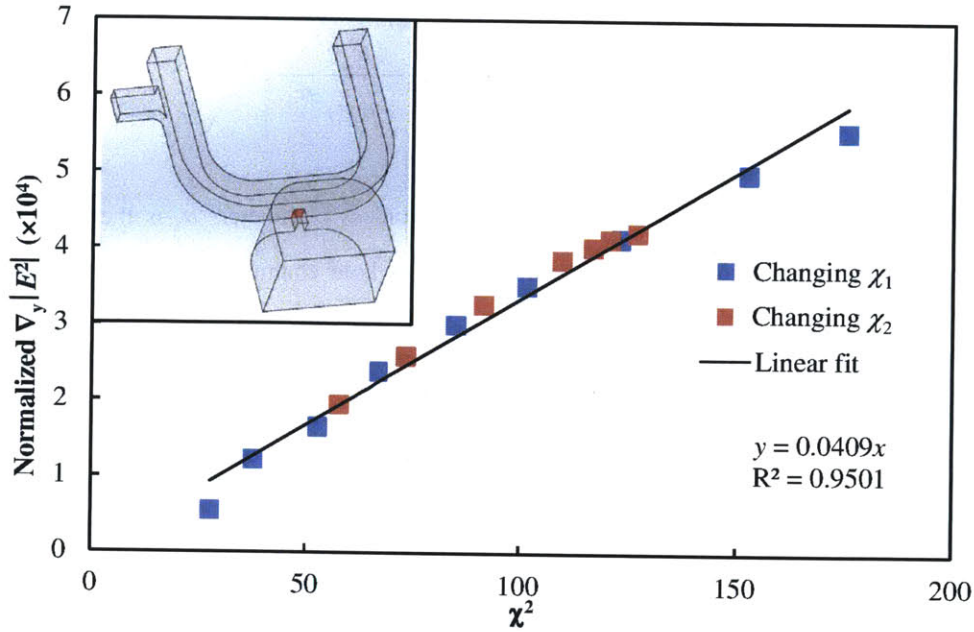


Figure 4-3 Relationship between the normalized y-component of $\nabla |E^2|$ and the effective constriction ratio squared. Square markers show the COMSOL simulation results of $\nabla_y |E^2|$ due to the variation of χ^2 via changing χ_1 (blue) and χ_2 (red). The upper left inset demonstrates the area (red) selected for averaging $\nabla_y |E^2|$.

4.3.2 Parallel hydraulic resistor model

Although the electric field gradient increases with the effective constriction ratio, the cross-sectional area of the constriction should not be arbitrarily small. Considering the flow field in the microchannel as a parallel hydraulic resistance circuit of the two outlet channels (**Figure 4-4**), the hydraulic resistance of the constriction, R_{h0} , should not be too high, otherwise few particles can get through the constriction, regardless of their polarizability. A proper case is that the ratio between the hydraulic resistances of the upper and lower outlets, $R_{h1}/(R_{h0}+R_{h2})$, and the ratio between the flow rates at the particle and sheath flow inlets, Q_p/Q_{sheath} , are of the same order.

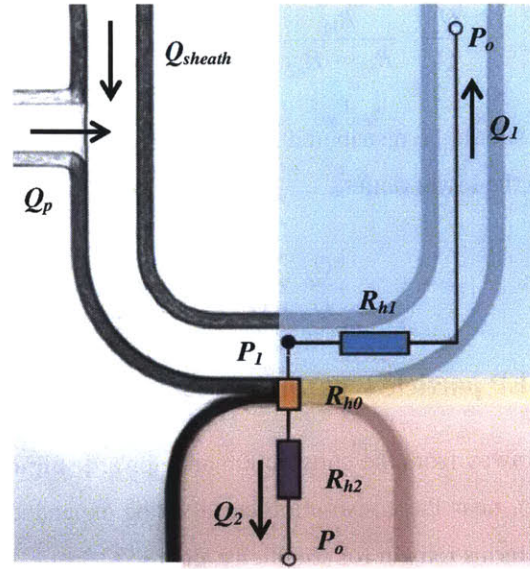


Figure 4-4 Schematic for the parallel hydraulic resistor model to evaluate the impact of the insulating channel geometry on the fluid field. R_h is the hydraulic resistance, while the subscripts, 0, 1, 2, denote the constriction, the upper outlet, and the lower outlet, respectively. Q_p , Q_{sheath} , Q_1 , and Q_2 are namely flow rates at the particle inlet, sheath flow inlet, upper outlet, and lower outlet. P_1 and P_o denote the pressures at the corresponding notes.

Neglecting the local hydraulic resistance caused by the dissipation of mechanical energy, the hydraulic resistance of each channel branch mainly attributes to momentum transfer to the channel walls. Based on the electric-hydraulic analogy, the hydraulic resistance (R_h) of laminar incompressible fluid in low Re microchannels can be considered as a constant for a given temperature and channel geometry, given by

$$R_h = (f \text{ Re}) \frac{\mu L}{2D_h^2 A}, \quad (4.6)$$

where f is the friction factor of the channel; L , A , and D_h denote the length, cross-sectional area, and hydraulic diameter of the channel; as well as μ is the fluid viscosity. For the whole 3DiDEP device, variation of f and Re for each branch is negligible, giving

$$R_h \sim \frac{LP^2}{A^3}, \quad (4.7)$$

where P is the wetted channel perimeter. Assuming that both the upper and lower outlets are connected to the ambient pressure, P_o (**Figure 4-4**),

$$\frac{Q_2}{Q_1} = \frac{R_{h1}}{R_{h0} + R_{h2}} \cong \frac{\alpha_1/\chi_1}{\alpha_0 + \alpha_2/\chi_2} = \beta. \quad (4.8)$$

The hydraulic resistance should be distributed in such a way that all streams originating from the particle inlet terminate in the lower outlet,

$$\frac{Q_2}{Q_1} \geq \frac{Q_p}{Q_{sheath}}. \quad (4.9)$$

4.3.3 Criteria of 3DiDEP particle separation

Let y denote the distance away from the constriction and upward (**Figure 4-2**). The DEP velocity in the y direction, $u_{DEP}(y)$, near the constriction can then be expanded in a series solution in y , where only the first three terms remain for simplicity, giving,

$$u_{DEP}(y) = \mu_{DEP} \nabla_y |E^2| \cong \frac{\mu_{DEP}}{w_0} \left(\frac{V_0}{L} \right)^2 \chi^2 \left(1 - \frac{2y}{w_1} + \frac{y^2}{w_1^2} \right), \quad (4.10)$$

where w_0 and w_1 are the widths of the constriction and channel 1 (**Figure 4-2**). For a particle to be deflected to the upper outlet, near the constriction it needs to be bumped out of the flow terminating in the lower outlet and displaced in the y direction a distance of w_0 , requiring time,

$$\tau_{DEP} = \int_0^{w_0} \frac{dy}{u_{DEP}(y)} = \frac{1}{\mu_{DEP} \chi^2} \left(\frac{L}{V_0} \right)^2 \frac{w_0^2}{1 - w_0/w_1}, \quad (4.11)$$

where τ_{DEP} is comparable to the time scale for the particle to migrate along the streamlines due to Stokes' drag. This longitudinal migration time, τ_D , is expected to be measured over the replacement of the total fluid volume in the constriction, giving

$$\tau_D \cong \frac{L_0 A_0}{Q_2} = \left(\frac{\alpha_0 \chi_1}{\alpha_1 \chi} + \frac{1}{2} \right) \frac{L_0 A_0}{Q}, \quad (4.12)$$

with Q being the total inlet flow rate, i.e. $Q = Q_p + Q_{sheath}$. Therefore, considering the requirement, $\tau_{DEP} \leq \tau_D$, and Eqn. (4.9), the criterion for particle deflection is

$$\lambda = \frac{Q}{\alpha_0 L \mu_{DEP}} \left(\frac{L}{V_0} \right)^2 \frac{\beta}{\chi^2} \leq 1, \quad \left(\beta \geq \frac{Q_p}{Q_{sheath}} \right). \quad (4.13)$$

Eqn. (4.13) suggests that the sorting sensitivity of the 3DiDEP device is facilitated by decreasing $\frac{\beta}{\chi^2}$. Compared to two dimensional iDEP systems, χ can be increased by an order of magnitude in 3DiDEP devices, and thus enables particle separation with high sensitivity. Additionally, with a given channel geometry and flow rate, the critical electric field intensity for the deflection of particle motion is given by,

$$E_c = \sqrt{\frac{Q}{\alpha_0 L \mu_{DEP}} \frac{\beta}{\chi^2}}, \quad (4.14)$$

which is inversely proportional to the particle diameter and square root of $|\kappa_{CM}|$. According to the geometric conditions of the 3DiDEP device demonstrated in Chapter 3 and assuming a 0.6 $\mu\text{L}/\text{min}$ total flow rate, the sorting parameter, λ , is calculated with different particle diameters (**Figure 4-5**). For separation of particles based on their size, the applied electric field should be chosen within the range where $\lambda \leq 1$ for large particles but $\lambda \geq 1$ for small ones (green region in **Figure 4-5**). However, it should be noted that there is an additional upper limit of the applied electric field due to thermal effects, which will be discussed in section 4.4.

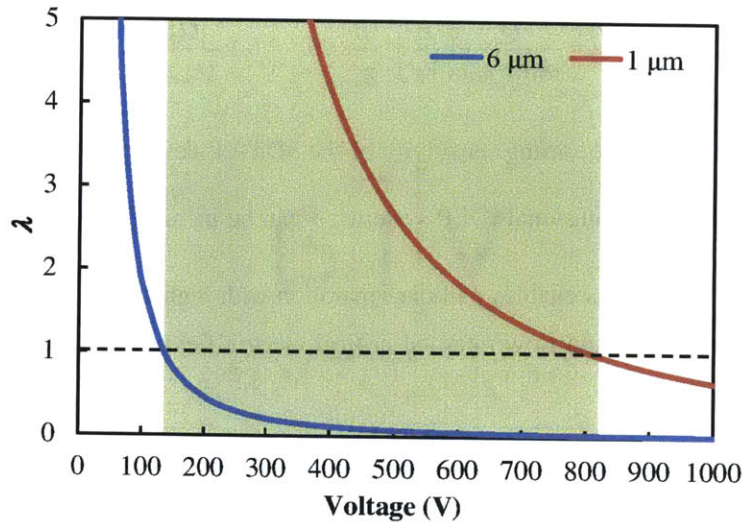


Figure 4-5 Sorting parameter calculated for particles with diameters of 6 μm (blue) and 1 μm (red). The Clausius-Mossotti factor is expected to be -0.5 for polystyrene beads.

4.4 Numerical modeling

Two numerical models were built using the COMSOL modeling environment. First, neglecting the electrothermal effects, the decoupled electric and flow fields were modeled only within the fluid phase using the electric current and creeping flow modules, respectively. Then, a time-dependent particle tracing step was computed with the results from the previous stationary step to predict the particle motion. Second, in order to evaluate the effects of electrothermal flow and joule heating effects, a 3D coupled electrothermal flow model was established, which captures both the fluid and PMMA substrate phases.

4.4.1 Prediction of particle trajectories

The computational domain considered for the particle trajectory model is restricted to the fluid phase in a portion of the 3DiDEP channel. As shown in **Figure 4-6** the 3D geometry was meshed with tetrahedral meshes. Since the electric field near the constriction is amplified by a ratio of χ (section 4.3.1) and the DEP force is proportional to the electric field squared, any minor errors in the electric field at the constriction result in a large error in the predicted particle motion. Therefore, the constriction is more densely meshed with an average element size less than 1 μm . The simulation was validated by increasing the number of mesh elements until there is no noticeable change in the results. The whole domain consists of more than 900,000 elements.

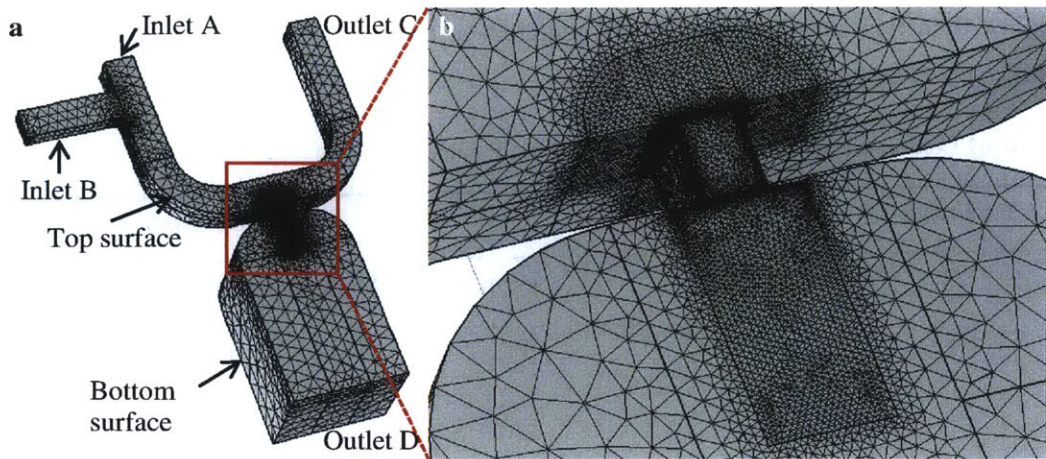


Figure 4-6 Meshed computational domain with labeled surface and boundaries.

This decoupled model for particle motion prediction consists of a stationary step for computing the distribution of the electric field and the flow field, and a time-dependent step for computing the particle trajectories. The stationary step was operated first and the results were saved as the input for the time-dependent step. All the constants and material properties used in the COMSOL numerical modeling are summarized in **Table 4.1**. The boundary conditions for the stationary step of the particle trajectory model are listed in **Table 4.2**. An RMS voltage difference of 150 V is applied across the entire channel. However, considering the voltage drop due to the extended channels connecting to the reservoirs (not included in the computational domain), the actual prescribed voltage at Inlet A and Outlet C is 66% of the potential value at the positive electrodes. This approximation is verified in the electrothermal flow model where the entire channel geometry was captured in the computational domain. Outlet D is electrically grounded. For the fluid flow conditions, the particle suspension is pumped into Inlet B with a constant 0.15 $\mu\text{L}/\text{min}$ flow rate. The particle and sheath flow are applied by the same syringe pump using two glass syringes with inner diameters of 1.03 and 2.3 mm, respectively. Thus, the ratio between the volumetric inflow rates at Inlet A and Inlet B is $(2.3/1.03)^2$. At the two outlets, the pressure is set to equal the reference pressure. With the assumptions of no electroosmosis, a non-slip wall boundary condition was applied to the remaining channel walls. Results demonstrating the 2D distribution of electric field and fluid field over the horizontal plane at the center of the constriction are shown in **Figure 4-7a** and **4-7b**. It is clear that the 3D insulating constriction generates a sharp electric field gradient in its vicinity. Additionally, the channel geometric and

applied fluid flow conditions satisfy the requirement that all the streams originating from the particle inlet terminate in the lower outlet.

Table 4.1 Constants and parameters used in the 3DiDEP numerical model

Parameter	Value	Unit	Description
ρ	997	kg/m ³	Medium density
η	0.9×10^{-3}	Pa·s	Medium dynamic viscosity
ϵ_m	80	1	Medium relative permittivity
ϵ_0	8.854×10^{-12}	F/m	Permittivity of free space
ϵ_p	2.5	1	Particle relative permittivity
σ_m	500	$\mu\text{S/cm}$	Medium electric conductivity
σ_p	0	$\mu\text{S/cm}$	Particle electric conductivity
T_0	293.15	K	Reference temperature
α_T	-0.0046	1/K	Temperature coefficient of fluid permittivity
β_T	0.02	1/K	Temperature coefficient of fluid electric conductivity
C_p	4.186	kJ/(kg·K)	Fluid heat capacity
k	0.6	W/(m·K)	Fluid thermal conductivity
C_{pPMMA}	1.42	kJ/(kg·K)	PMMA heat capacity
k_{PMMA}	0.21	W/(m·K)	PMMA thermal conductivity
ρ_{PMMA}	1190	kg/m ³	PMMA density
d_1	6	μm	Diameter of polystyrene beads
d_2	1	μm	Diameter of polystyrene beads

Table 4.2 Boundary conditions for the stationary step of the particle trajectory model

Boundary	Prescription	Description
Inlet A	$V_{high}=150 \times 66\% [V_{rms}]$; $U_{sheath}=0.72 [\mu L/min]$.	Applied RMS voltage on the high potential side (considering the voltage drop of the rest of the channel connecting to the reservoirs); Sheath flow rate.
Inlet B	$U_{pr}=0.15 [\mu L/min]$	Flow rate of the particle inflow streams.
Outlet C	$V_{high}=150 \times 66\% [V_{rms}]$; $P_0=1 [atm]$.	Connected to the same electrode with the Inlet A; Ambient pressure condition.
Outlet D	$V_{low}=0$ (grounded); $P_0=1 [atm]$.	Applied RMS voltage on the low potential side; Ambient pressure condition.
Sidewalls, top and bottom surface	$n \cdot j = 0$; $u = 0$.	Insulating wall condition; Non-slip wall condition.

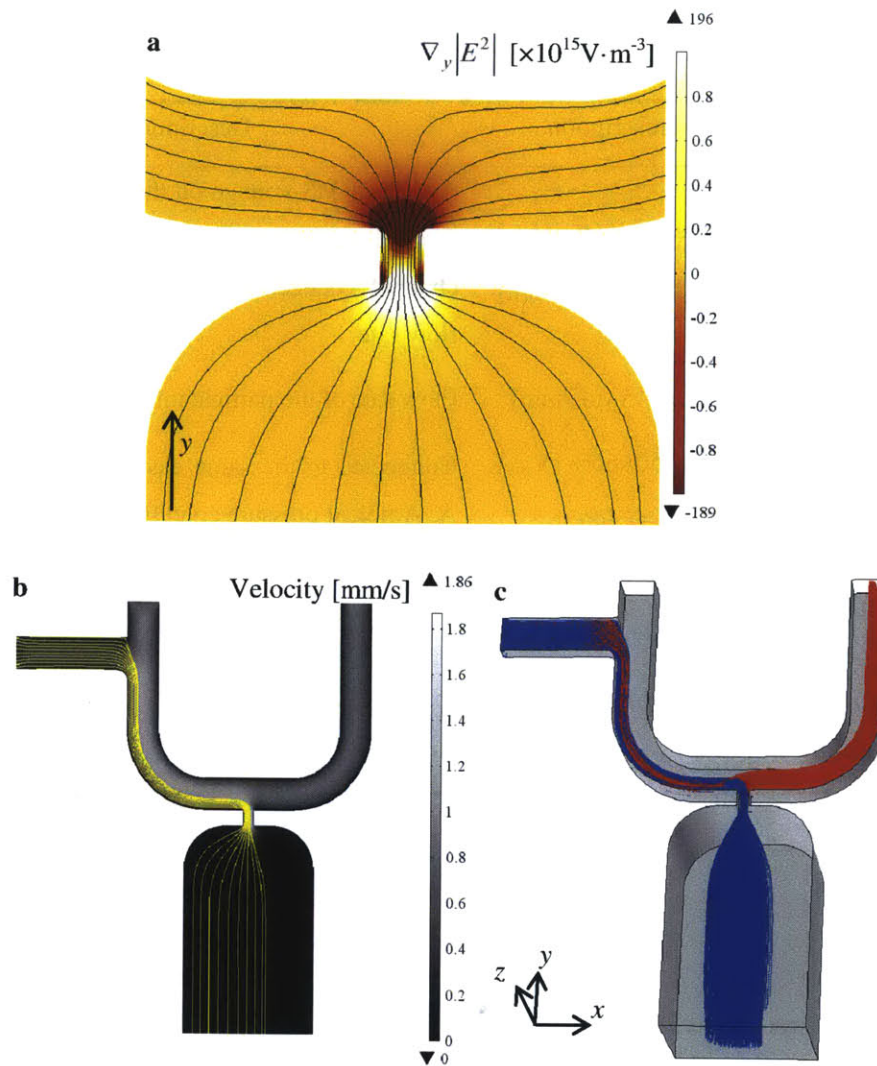


Figure 4-7 COMSOL simulation results showing the 2D distribution of the electric field (**a**) and the flow field (**b**) on the center horizontal plane of the constriction. (**a**) Solid black lines demonstrate the electric field lines, and the color scale illustrates the y-component of $\nabla |E^2|$ (unit: $\text{V} \cdot \text{m}^{-3}$). (**b**) Solid yellow lines show the streamlines originating from the particle inlet, and the gray scale shows the magnitude of flow velocity (unite: mm/s). (**c**) 3D trajectory prediction for polystyrene beads with diameters of 6 μm (red) and 1 μm (blue).

The particle trajectories were predicted using the fluid particle tracing module in COMSOL Multiphysics. A uniform particle distribution with a proper density was released at Inlet B from $t = 0$ with a local velocity distribution equal to the velocity field obtained from the previous step. In addition, the DEP force and drag force experienced by the particles were defined based on the electric field and flow field computed in the previous step. The electrophoretic force was assumed

negligible. A time-dependent solver was used to compute the particle motion for 50 sec with a time step less than 0.01 sec. The predicted particle trajectories are demonstrated in **Figure 4-7c**. The 6 μm particles (red) are estimated to be successfully separated from the 1 μm particles (blue) under the assumed conditions.

4.4.2 Prediction of electrothermal flow

In order to evaluate the effects of joule heating induced thermal flow and to determine the upper threshold of the applied electric field for efficient 3DiDEP sorting, an additional electrothermal flow model was conducted. A 3D stationary model was established to simulate the coupled electric field, heat transfer, and fluid flow using the conjugate heat transfer and electric current modules of COMSOL. The heat generation due to power dissipation of the electric field and heat flux due to the fluid flow impact the temperature distribution along the microchannel. On the other hand, the distribution of the temperature dependent fluid makes change to the electric field and fluid flow. Additionally, as noted in Eqn. (4.7), an electrothermal body force is experienced by the fluid. To determine the fully coupled electrothermal performance, the electric field, fluid flow, and the heat transfer were computed at the same time. **Figure 4-8a** demonstrates the labeled computational domain of both the fluid phase and the PMMA substrates (the top and bottom surfaces are set to be transparent for inner visualization). There is an array of three microchannels with a 7 mm space in between each two of the channels are fabricated on one PMMA chip, and only a portion of the PMMA device with one microchannel was captured in this model. Thus, the two vertical sidewalls normal to the y-axis are considered with a symmetric heat condition. Platinum electrodes with 0.25" diameter are assumed to be inserted half way down to the fluid body in the reservoirs. The constriction of the 3DiDEP channel was meshed with extremely fine mesh elements compared with the rest of the channel. Model validation was realized by increasing the mesh element number until there is no noticeable change in the results. The electric field was restricted within the fluid phase, while the heat transfer was computed over the entire domain. **Figure 4-8b** shows the RMS voltage distribution along the microchannel, and it verifies that 66% of the voltage difference across the whole channel was applied to the portion of the channel corresponding to the previous model for particle trajectory prediction.

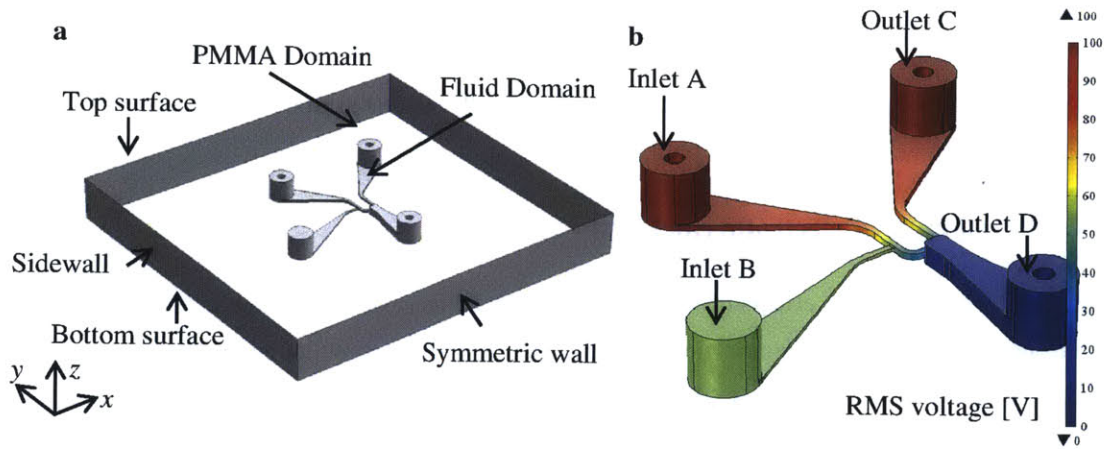


Figure 4-8 (a) Isometric view of the labeled computational domains and boundaries of the 3D electrothermal flow model. The surfaces normal to the x , y , and z axis are namely the PMMA sidewalls, symmetric vertical walls (considered as a plane of symmetry with no normal heat flux in between two microchannels), and top and bottom surfaces (transparent). (b) Volumetric RMS voltage distribution when a 100 V difference is applied across a microchannel. Also illustrated are the labeled opening boundaries of the fluid phase connecting to the external air.

Within the fluid domain, a heat source was defined equal to the energy dissipation of the electric field based on the result of the electric current module. The electrothermal force defined according to Eqn. (4.7) was applied to the fluid body. Convective heat flux conditions were applied to the top and bottom surfaces and sidewalls. The heat transfer coefficients are defined as functions in COMSOL and can be used directly for boundary conditions. For the top surface, the heat transfer coefficient

$$h_{top} = 0.54 \frac{k}{L} Ra_L^{1/4} \text{ for } Ra_L \text{ up to } 10^7 \quad (4.15)$$

$$h_{top} = 0.15 \frac{k}{L} Ra_L^{1/3} \text{ for } Ra_L > 10^7 \quad (4.16)$$

For the bottom surface,

$$h_{bottom} = 0.27 \frac{k}{L} Ra_L^{1/4} \quad (4.17)$$

And for side walls,

$$h_{sidewall} = \frac{k}{L} \left(0.68 + \frac{0.67Ra_L^{1/4}}{\left(1 + \left(\frac{0.492}{Pr} \right)^{9/16} \right)^{4/9}} \right) \text{ for } Ra_L \text{ up to } 10^7 \quad (4.18)$$

$$h_{sidewall} = \frac{k}{L} \left(0.825 + \frac{0.387Ra_L^{1/6}}{\left(1 + \left(\frac{0.492}{Pr} \right)^{9/16} \right)^{8/27}} \right)^2 \text{ for } Ra_L > 10^7 \quad (4.19)$$

Ra_L is the Raleigh number defined with respect to the characteristic length L , which is the ratio of the surface area to the perimeter for horizontal surfaces and the height for the vertical side walls. The thermal conductivity, k , and the Prandtl number, Pr , correspond to the external air. The vertical walls normal to the y -axis are considered as planes of symmetry, so that zero normal heat flux was prescribed. In addition, the open boundaries at the top surface of the reservoirs were prescribed with the ambient temperature. The boundary conditions for the electric field and fluid flow are the same with the decoupled model for particle trajectory prediction.

Various RMS voltage differences (50 V, 100V and 150 V) were applied to the boundaries corresponding to the electrode surfaces to evaluate the temperature and electrothermal flow distribution. **Figure 4-9** demonstrates the temperature change over the entire 3DiDEP device, showing that there can be a temperature increase in the constriction of the channel for about 20 K with an applied voltage above 150 V. This implies that in addition to the limitation of the applied voltage due to the requirements on hydraulic channel resistances, an extra limitation with lower maximum applied voltage arises in order to eliminate the electrothermal flow. The temperature variation along the centerline of the constriction in the y -direction (the origin lies in the center point of the constriction) is plotted in **Figure 4-9c**. The high temperature gradient near the constriction can induce an electrothermal flow comparable to the pressure driven flow. In **Figure 4-10a, c, and e** show the streamlines of purely the electrothermal flow with various RMS voltage differences applied across the channel. It is clear that under higher electric fields, rotating thermal flow may dominate the background fluid flow near the constriction region, and bring particles away from the constriction regardless of their polarizability. To compare between the pressure driven flow and electrothermal flow, superposition of the flow fields due to these two

mechanisms are plotted in **Figure 4-10b, d, and f**. As shown, with applied electric potential lower than 100 V, pressure driven flow dominates the background fluid motion, and the disturbances of the electrothermal flow can be neglected.

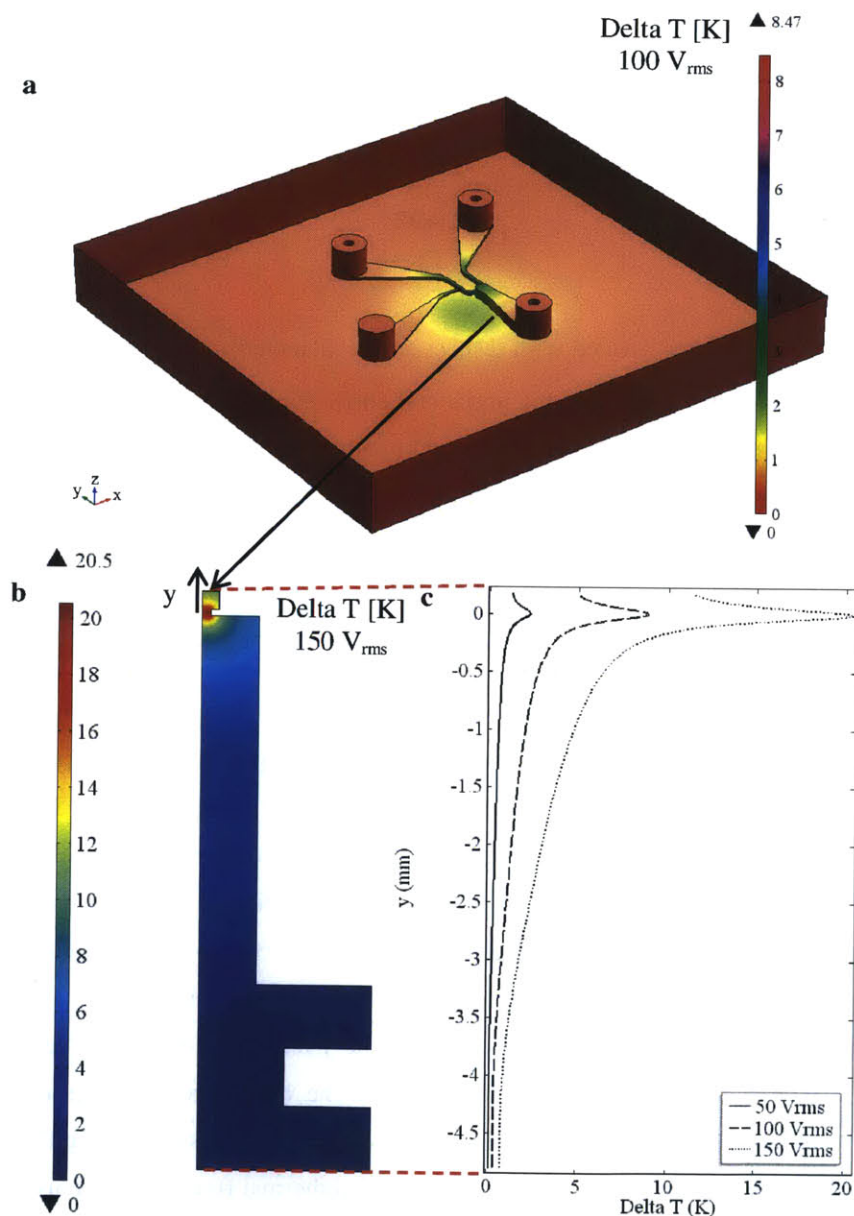


Figure 4-9 Temperature change (Delta T) along the microchannel with various voltages applied. (a) Volumetric delta T distribution over the fluid and PMMA domain when a 100 V difference is applied (transparent top surface) (b) 2D delta T distribution when a 150 V is applied on the plane across the center point of the constriction normal to the x-axis. (c) Temperature distribution along the centerline of the constriction in the y-direction when various voltages are applied.

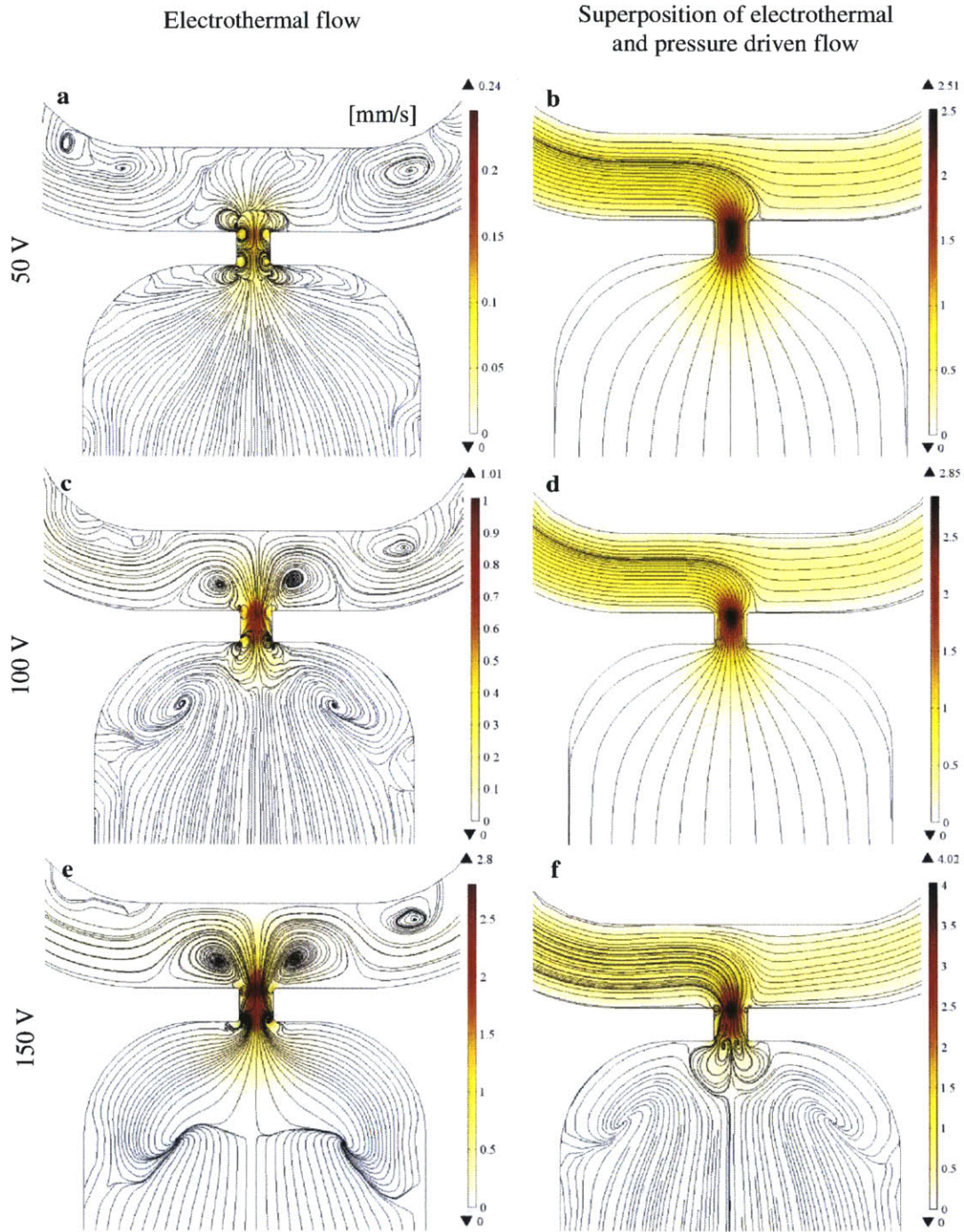


Figure 4-10 Streamlines of the fluid flow (solid lines) and distribution of velocity magnitude (color scale) when applied with RMS voltage differences of 50 V (a, b), 100 V(c, d) and 150 V (e, f). The cases of pure electrothermal flow are shown in (a, c, and e), while the interplayed cases involving both the pressure driven flow and the electrothermal flow are demonstrated in (b, d, and f).

Chapter 5

Continuous separation of particles based on size

5.1 Introduction

This chapter evaluates the potential of the described 3DiDEP device for continuous particle separation. In order to test the sensitivity of the 3DiDEP sorter demonstrated in Chapter 3 and validate the simulation results in Chapter 4, experiments were conducted using this 3DiDEP device to separate polystyrene beads with various diameters. A particle separation efficiency parameter was defined to evaluate the performance of 3DiDEP sorting. The preliminary experimental observation indicates that 3DiDEP is a powerful technique to achieve sensitive particle sorting without introducing strong joule heating issues. With further optimization of the device geometry, applied electric field frequency, and buffer composition, higher sorting sensitivity can be gained.

5.2 Methods and procedures

Suspensions of polystyrene beads with diameters of 1 and 6 μm were used to verify the 3DiDEP device sensitivity. 1 μm yellow-green FluoSpheres (Invitrogen, Eugene, OR, USA) and 6 μm red fluoresbrite microspheres (Polysciences, Warrington, PA, USA) were diluted and resuspended in a diluted Phosphate-Buffered Saline x1 (Mediatech, Manassas, VA, USA) buffer (DEP buffer) to make suspensions with a density of 3.6×10^6 and 3.54×10^6 particles per mL, respectively. The DEP buffer was measured to be 500 $\mu\text{S}/\text{cm}$ and pH 7 using a PC 510 bench pH/conductivity meter (Oakton, Vernon Hills, IL, USA). This condition was chosen to ensure a negative 0.5 value of the CM factor (κ_{CM}) at low frequency regime (**Figure 2-1 d**) while reducing temperature gradients across the channels. Before each experiment, 3DiDEP channels were flushed with 5 mL of 0.1 M potassium hydroxide (Sigma-Aldrich, St. Louis, MO, USA), deionized water, and DEP buffer in sequence with a flow rate of 0.5 mL/min using a Pico Plus Elite syringe pump (Harvard Apparatus, Holliston, MA, USA) to eliminate any surface charge impurities on the inner channel wall.

After the dynamic channel surface conditioning process, the 3DiDEP chip was loaded onto the stage of a Nikon Eclipse Ti inverted fluorescence microscope (Nikon Instruments, Melville, NY, USA) (Figure 5-1 a). Bubbles were carefully driven out of the channels by injecting fresh DEP buffer into one of the reservoirs using a pipette. Then the DEP buffer and particle suspension were pumped into the microchannel through inlet A and inlet B (Figure 5-1 b) using 50 μL and 250 μL glass syringes (Hamilton, Reno, NV, USA), respectively, with a total flow rate of 72 nL/hr. Given the different inner diameters of the 50 μL and 250 μL glass syringes, the flow rate of the buffer sheath flow is 5 times higher than that of the particle inflow, in order to effectively focus the bead stream towards the vicinity of the constriction.

Two sets of experiments were conducted to evaluate the performance of the 3DiDEP device. First, the 3DiDEP devices were tested separately with 1 and 6 μm particles. An AC sinusoidal signal with a frequency of 500 Hz was applied to the electrodes inserted in inlet A and outlet C, while outlet D was grounded. Three different voltage levels with root mean square values of 64 V (low), 81 V (medium), and 99 V (high) were applied across the channels using a waveform generator (Agilent Technologies, Santa Clara, CA, USA) and a high voltage amplifier (Trek, Lockport, NY, USA). Then with the same experimental conditions, the DEP response of a mixture of the two-sized beads was observed. Each test was repeated in triplicate. Fluorescence time-lapse image sequences were collected by a CoolSNAP HQ² cooled CCD camera (Photometrics, Tucson, AZ, USA) controlled by a Micro-Manager multi-acquisition package.

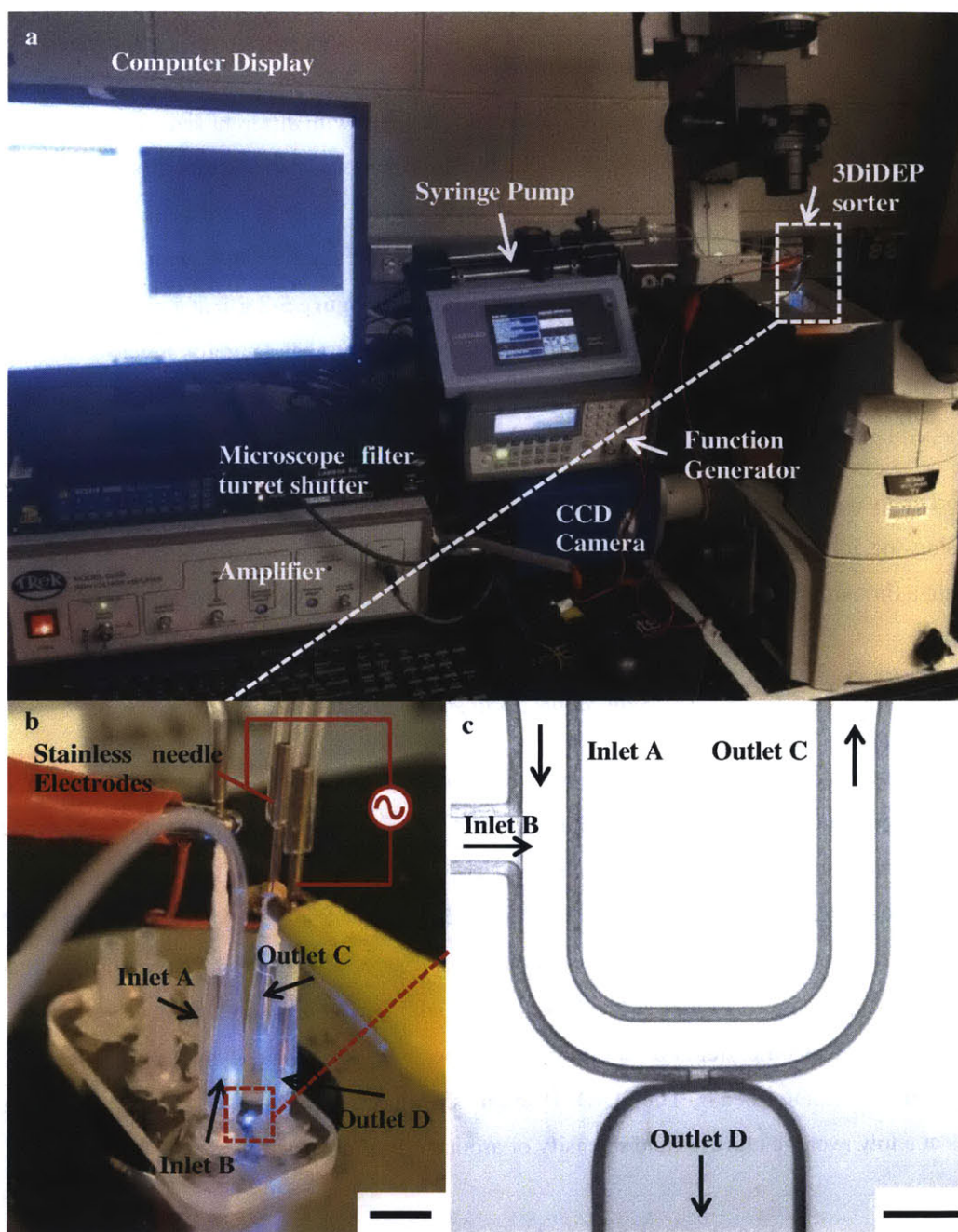


Figure 5-1 (a) Experimental setup for 3DiDEP particle sorting. (b) Photograph of a 3DiDEP chip with an array of three microchannels. An AC sinusoidal signal with a frequency of 500 Hz was applied via the stainless needles. DEP buffer and bead suspensions were introduced into inlet A and inlet B, respectively, using syringe pump, while separated samples were collected at outlet C and outlet D. (c) Micrograph of the 3DiDEP channel geometry. Scale bar, (b) 1 cm, (c) 200 μm .

5.3 3DiDEP device assessment with polystyrene microspheres

Figure 5-2 displays the motion of polystyrene microspheres with different sizes in the vicinity of the constriction when various voltages were applied. We observed throughout all the experiments that more particles were deflected towards the upper outlet C with an increasing applied electric field. However, under the same electric field conditions, more 6 μm particles can be deflected due to stronger negative DEP than 1 μm particles. As shown in **Figure 5-2 g-i**, at a given electric field, the majority of 6 μm beads (red) near the constriction travel laterally towards the upper streamlines while most of their smaller counterparts (green) are not deflected, leading to two enriched large and small particle outflow streams at outlet C and outlet D, respectively.

In order to quantitatively evaluate the particle separation purity of this 3DiDEP device, beads passing the inlet and outlet C, illustrated in dashed red boxes in **Figure 5-2 a**, were counted within a time-duration of 3 min. A sorting efficiency parameter, α , is defined as

$$\alpha = \frac{\text{Number of particles counted at outlet}}{\text{Number of particles counted at inlet}} \quad (5.1)$$

The parameter, α , was calculated and averaged from each triplicated set of experiments, and is shown in percentages in **Figure 5-3**, with error bars representing a standard deviation. **Figure 5-3 a** shows α calculated from experiments conducted with pure 6 μm (red) and 1 μm (green) bead suspensions, which are corresponding to **Figure 5-2 a-c** and **d-f**, respectively. **Figure 5-3 b** displays α extracted from experiments separating a mixture of the 6 μm (red) and 1 μm (green) beads, corresponding to **Figure 5-2 g-i**. It consists with our prediction that α increases with the raising applied electric field. In addition, larger beads experiencing stronger DEP leads to a higher α than smaller beads. The 3DiDEP sorter is available to separate 6 μm beads from 1 μm ones at a low average electric field intensity of around 100 V/cm.

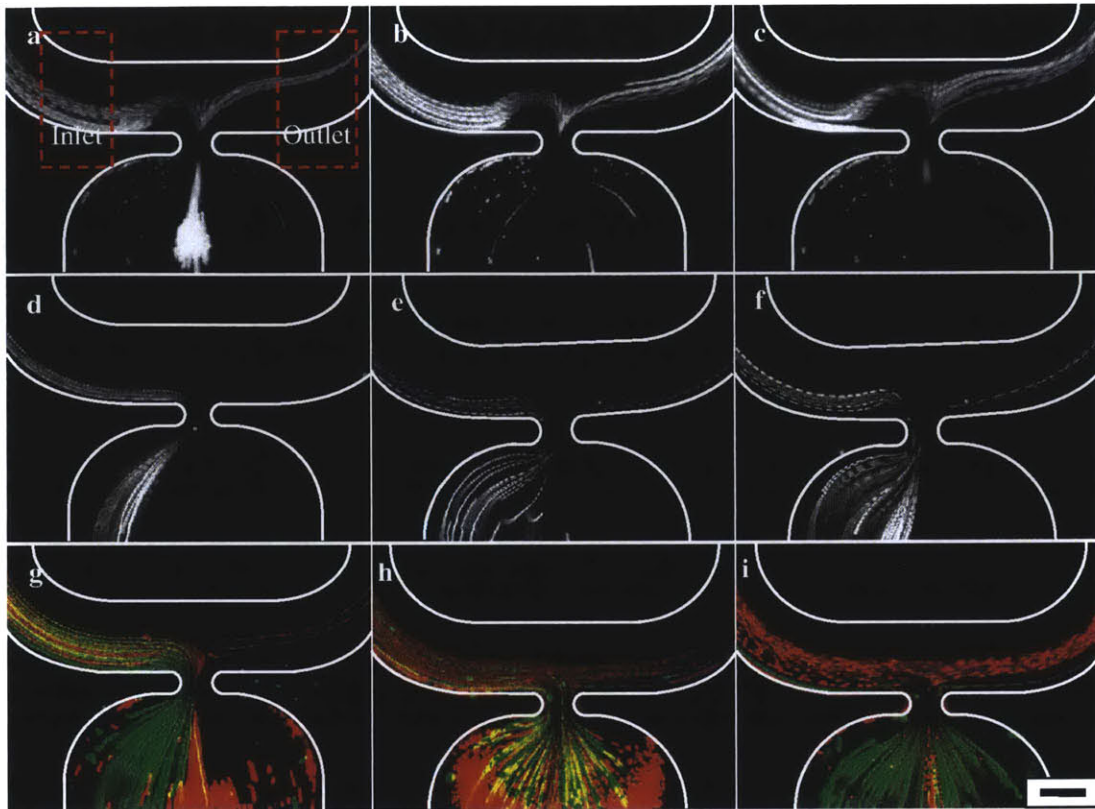


Figure 5-2 Fluorescence time-lapse image sequences for motion of (a-c) 6 μm beads, (d-f) 1 μm beads, and (g-i) both large (red) and small (green) beads in a mixture near the constriction region. Each experiment was conducted in triplicate under a 500 Hz AC signal with root mean square voltages of (a, d, and g) 64 V, (b, e, and h) 81 V, and (c, f, and i) 99V. Scale bar, 100 μm .

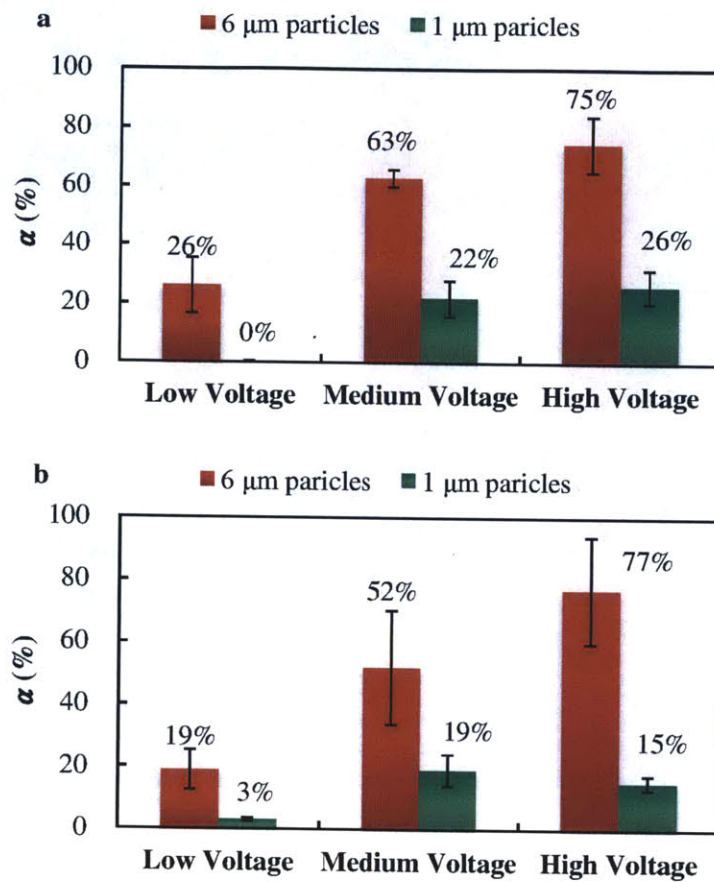


Figure 5-3 Sorting efficiency parameter α calculated from (a) experiments conducted with 6 μm beads (red) and 1 μm beads (green) separately, and (b) experiments conducted with a mixture of large (red) and small (green) beads.

Chapter 6

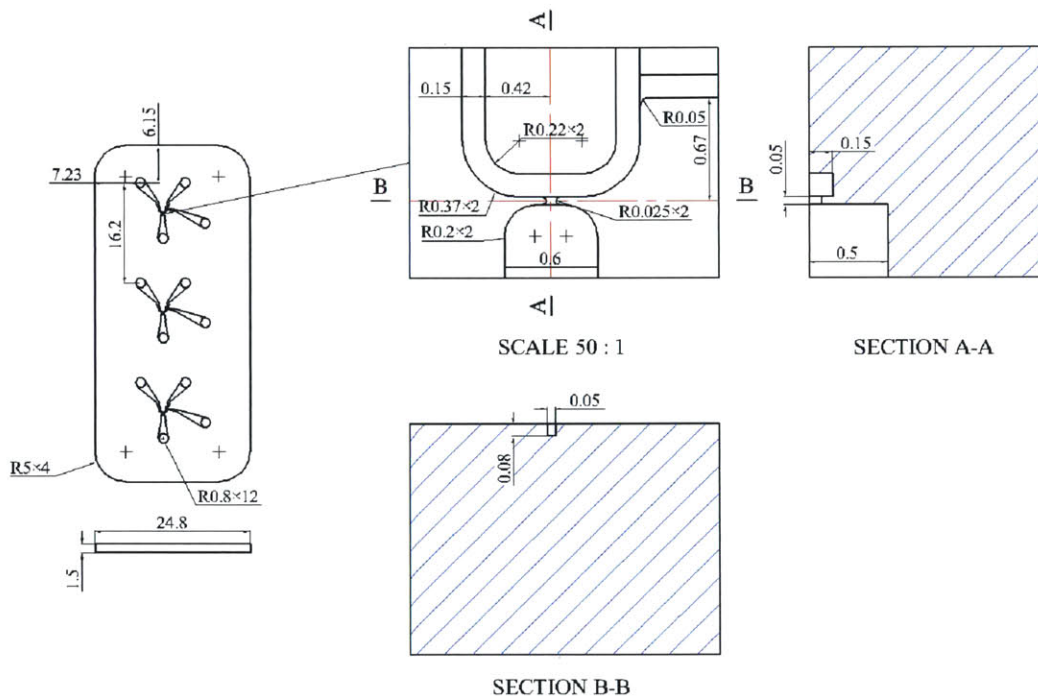
Conclusion and future work

A low frequency 3DiDEP microfluidic device was developed for continuous particle separation. The device was fabricated using a CNC micro milling technique and the sorting efficiency was assessed using experiments on polystyrene beads. A three dimensional insulating constriction was designed in the channel to create a large electric field gradient and achieve higher sorting sensitivity. The results of numerical modeling in chapter 4 and the experimental observation in chapter 5 show that particles with various sizes can be continuously isolated into two streams at the outlets without inducing strong joule heating and electrothermal flow effects. In addition, the sorting purity can be increased up to 77% when a 100 V/cm average electric field is applied.

However, there are still opportunities for future work on improvement of the separation sensitivity and extending the device to live cells. Considering that the DEP force is proportional to the volume of the cells, successful isolation of bacterial cells with diameters typically around 1-2 μm necessitates the improvement of sorting sensitivity. In addition, although the selective immobilization of bacteria in sub-strain level has been achieved using 3DiDEP, there are still challenges in continuous separation due to the significant drop of time scale for DEP force to act on the cells. This 3DiDEP device can be improved in several ways. First, the channel geometry can be further optimized by controlling the effective constriction ratio, χ , to reduce the required threshold electric field. Second, further investigation to optimize the buffer composition and applied frequency range is also helpful to strengthen the cell surface DEP response. In addition, in order to increase the time scale for DEP to act on the particles without increasing joule heating, a potential method is to integrate the DEP response of the particles multiple times. This could be achieved by extending the constriction geometry into an array or driving the cells of interest by the constriction region repeatedly. Furthermore, the accuracy of using fluorescence visualization to detect the cells at the outlet of the 3DiDEP device can be limited by multiple aspects, including the resolution of the microscope and the staining procedure. One possible label free method to improve the detecting sensitivity can be continuous measurement of the impedance at the channel outlet²⁷.

Appendix A

Design of the 3DiDEP microfluidic device for continuous particle separation (machined PMMA surface)



Appendix B

Machine code for 3DiDEP microdevice

(PROGRAM NAME_3DiDEP_Sorter)	Y-1.03
T1 M06	x-29
G120 B1 H1	Y0.24
G123 H1 W1 X2 Y0	x29
M05	Y1.51
G0 Z40	x-29
	Y2.78
N1(T1 1.5875 FLAT ENDMILL H1)	x29
T1 M06	Y4.05
G120 B1 H1	x-29
G54	Y5.32
G43 H1	x29
S48000 M03	Y6.59
M8	x-29
M0	Y7.86
G0 Z1	x29
G0 x-29 Y-15	Y9.13
G1 Z0 F600	x-29
x29	Y10.4
Y-13.73	x29
x-29	Y11.67
Y-12.46	x-29
x29	Y12.94
Y-11.19	x29
x-29	Y14.21
Y-9.92	x-29
x29	Y15.48
Y-8.65	x29
x-29	Z1
Y-7.38	
x29	G0 Z1
Y-6.11	G0 X-20.035 Y-4.544
x-29	G1 Z-1.62 F75
Y-4.84	Z1
x29	G0 Y2.656
Y-3.57	G1 Z-1.62 F75
x-29	Z1
Y-2.3	G0 X-16.182 Y4.601
x29	G1 Z-1.62 F75

Z1
G0 X-11.409 Y2.656
G1 Z-1.62 F75
Z1
G0 Y-4.544
G1 Z-1.62 F75
Z1

G0 X-4.313
G1 Z-1.62 F75
Z1
G0 Y2.656
G1 Z-1.62 F75
Z1
G0 X-.46 Y4.601
G1 Z-1.62 F75
Z1
X4.313 Y2.656
G1 Z-1.62 F75
Z1
G0 Y-4.544
G1 Z-1.62 F75
Z1

G0 X11.409
G1 Z-1.62 F75
Z1
G0 Y2.656
G1 Z-1.62 F75
Z1
G0 X15.262 Y4.601
G1 Z-1.62 F75
Z1
G0 X20.035 Y2.656
G1 Z-1.62 F75
Z1
G0 Y-4.544
G1 Z-1.62 F75
Z1

G0 Z70
G0 X0 Y0
M5
M09

N1(T1 | 0.1016 FLAT ENDMILL | H1)
T1 M06
G120 B1 H1
G54

G43 H1
S48000 M03
M8
M0

G00 X-19.997 Y-4.494
G0 Z1
G1 Z-.075 F200.
X-19.979 Y-4.516
X-16.497 Y-1.596
G2 X-16.393 Y-1.558 I104 J-.123
G1 X-16.007
G3 X-15.818 Y-1.369 I0. J.189
G1 Y-.519
G3 X-16.007 Y-.33 I-.189 J0.
G1 X-16.057
G2 X-16.168 Y-.219 I0. J.111
G1 Y4.54
X-16.196
Y-.269
G2 X-16.257 Y-.33 I-.061 J0.
G1 X-16.393
G2 X-16.497 Y-.292 I0. J.161
G1 X-19.979 Y2.628
X-19.997 Y2.606
X-16.515 Y-.314
G3 X-16.393 Y-.358 I.122 J.145
G1 X-16.007
G2 X-15.846 Y-.519 I0. J-.161
G1 Y-1.369
G2 X-16.007 Y-1.53 I-.161 J0.
G1 X-16.393
G3 X-16.515 Y-1.574 I0. J-.189
G1 X-19.997 Y-4.494
G1 Z-.08 F50.
X-20.012 Y-4.493
X-19.98 Y-4.53
X-16.49 Y-1.603
G2 X-16.393 Y-1.568 I097 J-.116
G1 X-16.007
G3 X-15.808 Y-1.369 I0. J.199
G1 Y-.519
G3 X-16.007 Y-.32 I-.199 J0.
G1 X-16.057
G2 X-16.158 Y-.219 I0. J.101
G1 Y4.55
X-16.206
Y-.269
G2 X-16.257 Y-.32 I-.051 J0.

G1 X-16.393
G2 X-16.49 Y-.284 IO. J.151
G1 X-19.98 Y2.642
X-20.012 Y2.605
X-16.521 Y-.321
G3 X-16.393 Y-.368 I.128 J.152
G1 X-16.007
G2 X-15.856 Y-.519 IO. J-.151
G1 Y-1.369
G2 X-16.007 Y-1.52 I-.151 JO.
G1 X-16.393
G3 X-16.521 Y-1.566 IO. J-.199
G1 X-20.012 Y-4.493
G1 Z1.

G00 X-11.465 Y-4.516
G1 Z-.075 F200.
X-11.447 Y-4.494
X-14.929 Y-1.574
G3 X-15.051 Y-1.53 I-.122 J-.145
G1 X-15.437
G2 X-15.598 Y-1.369 IO. J.161
G1 Y-.519
G2 X-15.437 Y-.358 I.161 JO.
G1 X-15.051
G3 X-14.929 Y-.314 IO. J.189
G1 X-11.447 Y2.606
X-11.465 Y2.628
X-14.947 Y-.292
G2 X-15.051 Y-.33 I-.104 J.123
G1 X-15.437
G3 X-15.626 Y-.519 IO. J-.189
G1 Y-1.369
G3 X-15.437 Y-1.558 I.189 JO.
G1 X-15.051
G2 X-14.947 Y-1.596 IO. J-.161
G1 X-11.465 Y-4.516
G1 Z-.08 F50.
X-11.464 Y-4.53
X-11.433 Y-4.493
X-14.923 Y-1.566
G3 X-15.051 Y-1.52 I-.128 J-.153
G1 X-15.437
G2 X-15.588 Y-1.369 IO. J.151
G1 Y-.519
G2 X-15.437 Y-.368 I.151 JO.
G1 X-15.051
G3 X-14.923 Y-.321 IO. J.199
G1 X-11.433 Y2.605

X-11.464 Y2.642
X-14.954 Y-.284
G2 X-15.051 Y-.32 I-.097 J.115
G1 X-15.437
G3 X-15.636 Y-.519 IO. J-.199
G1 Y-1.369
G3 X-15.437 Y-1.568 I.199 JO.
G1 X-15.051
G2 X-14.954 Y-1.603 IO. J-.151
G1 X-11.464 Y-4.53
G1 Z1.

G00 X-4.275 Y-4.494
G0 Z1
G1 Z-.075 F200.
X-4.257 Y-4.516
X-.775 Y-1.596
G2 X-.671 Y-1.558 I.104 J-.123
G1 X-.285
G3 X-.096 Y-1.369 IO. J.189
G1 Y-.519
G3 X-.285 Y-.33 I-.189 JO.
G1 X-.335
G2 X-.446 Y-.219 IO. J.111
G1 Y4.54
X-.474
Y-.269
G2 X-.535 Y-.33 I-.061 JO.
G1 X-.671
G2 X-.775 Y-.292 IO. J.161
G1 X-4.257 Y2.628
X-4.275 Y2.606
X-.793 Y-.314
G3 X-.671 Y-.358 I.122 J.145
G1 X-.285
G2 X-.124 Y-.519 IO. J-.161
G1 Y-1.369
G2 X-.285 Y-1.53 I-.161 JO.
G1 X-.671
G3 X-.793 Y-1.574 IO. J-.189
G1 X-4.275 Y-4.494
G1 Z-.08 F50.
X-4.289 Y-4.493
X-4.258 Y-4.53
X-.768 Y-1.603
G2 X-.671 Y-1.568 I.097 J-.116
G1 X-.285
G3 X-.086 Y-1.369 IO. J.199
G1 Y-.519

G3 X-.285 Y-.32 I-.199 J0.
G1 X-.335
G2 X-.436 Y-.219 IO. J.101
G1 Y4.55
X-.484
Y-.269
G2 X-.535 Y-.32 I-.051 J0.
G1 X-.671
G2 X-.768 Y-.284 IO. J.151
G1 X-4.258 Y2.642
X-4.289 Y2.605
X-.799 Y-.321
G3 X-.671 Y-.368 I.128 J.152
G1 X-.285
G2 X-.134 Y-.519 IO. J-.151
G1 Y-1.369
G2 X-.285 Y-1.52 I-.151 J0.
G1 X-.671
G3 X-.799 Y-1.566 IO. J-.199
G1 X-4.289 Y-4.493
G1 Z1.

G00 X4.257 Y-4.516
G1 Z-.075 F200.
X4.275 Y-4.494
X.793 Y-1.574
G3 X.671 Y-1.53 I-.122 J-.145
G1 X.285
G2 X.124 Y-1.369 IO. J.161
G1 Y-.519
G2 X.285 Y-.358 I.161 J0.
G1 X.671
G3 X.793 Y-.314 IO. J.189
G1 X4.275 Y2.606
X4.257 Y2.628
X.775 Y-.292
G2 X.671 Y-.33 I-.104 J.123
G1 X.285
G3 X.096 Y-.519 IO. J-.189
G1 Y-1.369
G3 X.285 Y-1.558 I.189 J0.
G1 X.671
G2 X.775 Y-1.596 IO. J-.161
G1 X4.257 Y-4.516
G1 Z-.08 F50.
X4.258 Y-4.53
X4.289 Y-4.493
X.799 Y-1.566
G3 X.671 Y-1.52 I-.128 J-.153

G1 X.285
G2 X.134 Y-1.369 IO. J.151
G1 Y-.519
G2 X.285 Y-.368 I.151 J0.
G1 X.671
G3 X.799 Y-.321 IO. J.199
G1 X4.289 Y2.605
X4.258 Y2.642
X.768 Y-.284
G2 X.671 Y-.32 I-.097 J.115
G1 X.285
G3 X.086 Y-.519 IO. J-.199
G1 Y-1.369
G3 X.285 Y-1.568 I.199 J0.
G1 X.671
G2 X.768 Y-1.603 IO. J-.151
G1 X4.258 Y-4.53
G1 Z1.

G00 X11.447 Y-4.494
G0 Z1
G1 Z-.075 F200.
X11.465 Y-4.516
X14.947 Y-1.596
G2 X15.051 Y-1.558 I.104 J-.123
G1 X15.437
G3 X15.626 Y-1.369 IO. J.189
G1 Y-.519
G3 X15.437 Y-.33 I-.189 J0.
G1 X15.387
G2 X15.276 Y-.219 IO. J.111
G1 Y4.54
X15.248
Y-.269
G2 X15.187 Y-.33 I-.061 J0.
G1 X15.051
G2 X14.947 Y-.292 IO. J.161
G1 X11.465 Y2.628
X11.447 Y2.606
X14.929 Y-.314
G3 X15.051 Y-.358 I.122 J.145
G1 X15.437
G2 X15.598 Y-.519 IO. J-.161
G1 Y-1.369
G2 X15.437 Y-1.53 I-.161 J0.
G1 X15.051
G3 X14.929 Y-1.574 IO. J-.189
G1 X11.447 Y-4.494
G1 Z-.08 F50.

X11.433 Y-4.493
X11.464 Y-4.53
X14.954 Y-1.603
G2 X15.051 Y-1.568 I.097 J-.116
G1 X15.437
G3 X15.636 Y-1.369 I. J.199
G1 Y-.519
G3 X15.437 Y-.32 I-.199 J0.
G1 X15.387
G2 X15.286 Y-.219 I. J.101
G1 Y4.55
X15.238
Y-.269
G2 X15.187 Y-.32 I-.051 J0.
G1 X15.051
G2 X14.954 Y-.284 I. J.151
G1 X11.464 Y2.642
X11.433 Y2.605
X14.923 Y-.321
G3 X15.051 Y-.368 I.128 J.152
G1 X15.437
G2 X15.588 Y-.519 I. J-.151
G1 Y-1.369
G2 X15.437 Y-1.52 I-.151 J0.
G1 X15.051
G3 X14.923 Y-1.566 I. J-.199
G1 X11.433 Y-4.493
G1 Z1.

G00 X19.979 Y-4.516
G1 Z-.075 F200.
X19.997 Y-4.494
X16.515 Y-1.574
G3 X16.393 Y-1.53 I-.122 J-.145
G1 X16.007
G2 X15.846 Y-1.369 I. J.161
G1 Y-.519
G2 X16.007 Y-.358 I.161 J0.
G1 X16.393
G3 X16.515 Y-.314 I. J.189
G1 X19.997 Y2.606
X19.979 Y2.628
X16.497 Y-.292
G2 X16.393 Y-.33 I-.104 J.123
G1 X16.007
G3 X15.818 Y-.519 I. J-.189
G1 Y-1.369
G3 X16.007 Y-1.558 I.189 J0.
G1 X16.393

G2 X16.497 Y-1.596 I. J-.161
G1 X19.979 Y-4.516
G1 Z-.08 F50.
X19.98 Y-4.53
X20.012 Y-4.493 F50.
X16.521 Y-1.566
G3 X16.393 Y-1.52 I-.128 J-.153
G1 X16.007
G2 X15.856 Y-1.369 I. J.151
G1 Y-.519
G2 X16.007 Y-.368 I.151 J0.
G1 X16.393
G3 X16.521 Y-.321 I. J.199
G1 X20.012 Y2.605
X19.98 Y2.642
X16.49 Y-.284
G2 X16.393 Y-.32 I-.097 J.115
G1 X16.007
G3 X15.808 Y-.519 I. J-.199
G1 Y-1.369
G3 X16.007 Y-1.568 I.199 J0.
G1 X16.393
G2 X16.49 Y-1.603 I. J-.151
G1 X19.98 Y-4.53
G1 Z1.

G0 Z70
G0 X0 Y0
M5
M09

N1(T1 | 0.0508 FLAT ENDMILL | H1)
T1 M06
G120 B1 H1
G54
G43 H1
S48000 M03
M8
M0
G0 Z1

G0 X-15.782 Y-.533
G1 Z0 F10.
G3 X-15.747 Y-.569 I.035 J0
G1 X-15.697
G3 X-15.662 Y-.533 I. J.036
G1 Y-.604
G3 X-15.697 Y-.569 I-.035 J0.
G1 X-15.747

G3 X-15.782 Y-.604 IO. J-.036
G1 Y-.533
Z-.03 F10.
G3 X-15.747 Y-.569 I.035 J0
G1 X-15.697
G3 X-15.662 Y-.533 IO. J.036
G1 Y-.604
G3 X-15.697 Y-.569 I-.035 J0.
G1 X-15.747
G3 X-15.782 Y-.604 IO. J-.036
G1 Y-.533
G1 Z1.

G0 X-15.782 Y-.783
G1 Z0 F10.
G3 X-15.747 Y-.819 I.035 J0
G1 X-15.697
G3 X-15.662 Y-.783 IO. J.036
G1 Y-.854
G3 X-15.697 Y-.819 I-.035 J0.
G1 X-15.747
G3 X-15.782 Y-.854 IO. J-.036
G1 Y-.783
Z-.03 F10.
G3 X-15.747 Y-.819 I.035 J0
G1 X-15.697
G3 X-15.662 Y-.783 IO. J.036
G1 Y-.854
G3 X-15.697 Y-.819 I-.035 J0.
G1 X-15.747
G3 X-15.782 Y-.854 IO. J-.036
G1 Y-.783
G1 Z1.

G0 X-15.782 Y-1.033
G1 Z0 F10.
G3 X-15.747 Y-1.069 I.035 J0
G1 X-15.697
G3 X-15.662 Y-1.033 IO. J.036
G1 Y-1.104
G3 X-15.697 Y-1.069 I-.035 J0.
G1 X-15.747
G3 X-15.782 Y-1.104 IO. J-.036
G1 Y-1.033
Z-.03 F10.
G3 X-15.747 Y-1.069 I.035 J0
G1 X-15.697
G3 X-15.662 Y-1.033 IO. J.036
G1 Y-1.104

G3 X-15.697 Y-1.069 I-.035 J0.
G1 X-15.747
G3 X-15.782 Y-1.104 IO. J-.036
G1 Y-1.033
G1 Z1.

G0 X-15.782 Y-1.283
G1 Z0 F10.
G3 X-15.747 Y-1.319 I.035 J0
G1 X-15.697
G3 X-15.662 Y-1.283 IO. J.036
G1 Y-1.354
G3 X-15.697 Y-1.319 I-.035 J0.
G1 X-15.747
G3 X-15.782 Y-1.354 IO. J-.036
G1 Y-1.283
Z-.03 F10.
G3 X-15.747 Y-1.319 I.035 J0
G1 X-15.697
G3 X-15.662 Y-1.283 IO. J.036
G1 Y-1.354
G3 X-15.697 Y-1.319 I-.035 J0.
G1 X-15.747
G3 X-15.782 Y-1.354 IO. J-.036
G1 Y-1.283
G1 Z1.

G0 X-.0604 Y-.533
G1 Z0 F10.
G3 X-.025 Y-.569 I.035 J0
G1 X.025
G3 X.0604 Y-.533 IO. J.036
G1 Y-.604
G3 X.025 Y-.569 I-.035 J0.
G1 X-.025
G3 X-.0604 Y-.604 IO. J-.036
G1 Y-.533
Z-.03 F10.
G3 X-.025 Y-.569 I.035 J0
G1 X.025
G3 X.0604 Y-.533 IO. J.036
G1 Y-.604
G3 X.025 Y-.569 I-.035 J0.
G1 X-.025
G3 X-.0604 Y-.604 IO. J-.036
G1 Y-.533
G1 Z1.

G0 X-.0604 Y-.783

G1 Z0 F10.
G3 X-.025 Y-.819 I.035 J0
G1 X.025
G3 X.0604 Y-.783 IO. J.036
G1 Y-.854
G3 X.025 Y-.819 I-.035 J0.
G1 X-.025
G3 X-.0604 Y-.854 IO. J-.036
G1 Y-.783
Z-.03 F10.
G3 X-.025 Y-.819 I.035 J0
G1 X.025
G3 X.0604 Y-.783 IO. J.036
G1 Y-.854
G3 X.025 Y-.819 I-.035 J0.
G1 X-.025
G3 X-.0604 Y-.854 IO. J-.036
G1 Y-.783
G1 Z1.

G0 X-.0604 Y-1.033
G1 Z0 F10.
G3 X-.025 Y-1.069 I.035 J0
G1 X.025
G3 X.0604 Y-1.033 IO. J.036
G1 Y-1.104
G3 X.025 Y-1.069 I-.035 J0.
G1 X-.025
G3 X-.0604 Y-1.104 IO. J-.036
G1 Y-1.033
Z-.03 F10.
G3 X-.025 Y-1.069 I.035 J0
G1 X.025
G3 X.0604 Y-1.033 IO. J.036
G1 Y-1.104
G3 X.025 Y-1.069 I-.035 J0.
G1 X-.025
G3 X-.0604 Y-1.104 IO. J-.036
G1 Y-1.033
G1 Z1.

G0 X-.0604 Y-1.283
G1 Z0 F10.
G3 X-.025 Y-1.319 I.035 J0
G1 X.025
G3 X.0604 Y-1.283 IO. J.036
G1 Y-1.354
G3 X.025 Y-1.319 I-.035 J0.
G1 X-.025

G3 X-.0604 Y-1.354 IO. J-.036
G1 Y-1.283
Z-.03 F10.
G3 X-.025 Y-1.319 I.035 J0
G1 X.025
G3 X.0604 Y-1.283 IO. J.036
G1 Y-1.354
G3 X.025 Y-1.319 I-.035 J0.
G1 X-.025
G3 X-.0604 Y-1.354 IO. J-.036
G1 Y-1.283
G1 Z1.

G0 X15.662 Y-.533
G1 Z0 F10.
G3 X15.697 Y-.569 I.035 J0
G1 X15.747
G3 X15.782 Y-.533 IO. J.036
G1 Y-.604
G3 X15.747 Y-.569 I-.035 J0.
G1 X15.697
G3 X15.662 Y-.604 IO. J-.036
G1 Y-.533
Z-.03 F10.
G3 X15.697 Y-.569 I.035 J0
G1 X15.747
G3 X15.782 Y-.533 IO. J.036
G1 Y-.604
G3 X15.747 Y-.569 I-.035 J0.
G1 X15.697
G3 X15.662 Y-.604 IO. J-.036
G1 Y-.533
G1 Z1.

G0 X15.662 Y-.783
G1 Z0 F10.
G3 X15.697 Y-.819 I.035 J0
G1 X15.747
G3 X15.782 Y-.783 IO. J.036
G1 Y-.854
G3 X15.747 Y-.819 I-.035 J0.
G1 X15.697
G3 X15.662 Y-.854 IO. J-.036
G1 Y-.783
Z-.03 F10.
G3 X15.697 Y-.819 I.035 J0
G1 X15.747
G3 X15.782 Y-.783 IO. J.036
G1 Y-.854

G3 X15.747 Y-.819 I-.035 J0.
G1 X15.697
G3 X15.662 Y-.854 I0. J-.036
G1 Y-.783
G1 Z1.

G0 X15.662 Y-1.033
G1 Z0 F10.
G3 X15.697 Y-1.069 I035 J0
G1 X15.747
G3 X15.782 Y-1.033 I0. J.036
G1 Y-1.104
G3 X15.747 Y-1.069 I-.035 J0.
G1 X15.697
G3 X15.662 Y-1.104 I0. J-.036
G1 Y-1.033
Z-.03 F10.
G3 X15.697 Y-1.069 I035 J0
G1 X15.747
G3 X15.782 Y-1.033 I0. J.036
G1 Y-1.104
G3 X15.747 Y-1.069 I-.035 J0.
G1 X15.697
G3 X15.662 Y-1.104 I0. J-.036
G1 Y-1.033
G1 Z1.

G0 X15.662 Y-1.283
G1 Z0 F10.
G3 X15.697 Y-1.319 I035 J0
G1 X15.747
G3 X15.782 Y-1.283 I0. J.036
G1 Y-1.354
G3 X15.747 Y-1.319 I-.035 J0.
G1 X15.697
G3 X15.662 Y-1.354 I0. J-.036
G1 Y-1.283
Z-.03 F10.
G3 X15.697 Y-1.319 I035 J0
G1 X15.747
G3 X15.782 Y-1.283 I0. J.036
G1 Y-1.354
G3 X15.747 Y-1.319 I-.035 J0.
G1 X15.697
G3 X15.662 Y-1.354 I0. J-.036
G1 Y-1.283
G1 Z1.

G0 Z70.
G0 X0 Y0
M5
M09
M30

Bibliography

- 1 ABRAMOWITZ, M. & STEGUN, I. A. 1965. *Handbook of mathematical functions, with formulas, graphs, and mathematical tables*, New York,, Dover Publications.
- 2 ANDERSON, J. R., CHIU, D. T., JACKMAN, R. J., CHERNIAVSKAYA, O., MCDONALD, J. C., WU, H. K., WHITESIDES, S. H. & WHITESIDES, G. M. 2000. Fabrication of topologically complex three-dimensional microfluidic systems in PDMS by rapid prototyping. *Analytical Chemistry*, 72, 3158-3164.
- 3 BARBULOVIC-NAD, I., XUAN, X., LEE, J. S. H. & LI, D. 2006. DC-dielectrophoretic separation of microparticles using an oil droplet obstacle. *Lab on a Chip*, 6, 274-279.
- 4 BASURAY, S. & CHANG, H. C. 2007. Induced dipoles and dielectrophoresis of nanocolloids in electrolytes. *Physical Review E*, 75.
- 5 BASURAY, S., WEI, H. H. & CHANG, H. C. 2010. Dynamic double layer effects on ac-induced dipoles of dielectric nanocolloids. *Biomicrofluidics*, 4.
- 6 BECKER, F. F., WANG, X. B., HUANG, Y., PETHIG, R., VYKOUKAL, J. & GASCOYNE, P. R. C. 1995. Separation of Human Breast-Cancer Cells from Blood by Differential Dielectric Affinity. *Proceedings of the National Academy of Sciences of the United States of America*, 92, 860-864.
- 7 BECKER, H. & HEIM, U. 2000. Hot embossing as a method for the fabrication of polymer high aspect ratio structures. *Sensors and Actuators a-Physical*, 83, 130-135.
- 8 BECKER, H. & LOCASCIO, L. E. 2002. Polymer microfluidic devices. *Talanta*, 56, 267-287.
- 9 BELL, G. I. 1978. Models for the specific adhesion of cells to cells. *Science*, 200, 618-27.
- 10 BHATTACHARYA, S., CHAO, T.-C. & ROS, A. 2011. Insulator-based dielectrophoretic single particle and single cancer cell trapping. *ELECTROPHORESIS*, 32, 2550-2558.
- 11 BRAFF, W. A., PIGNIER, A. & BUIE, C. R. 2012. High sensitivity three-dimensional insulator-based dielectrophoresis. *Lab Chip*, 12, 1327-31.
- 12 BRAFF, W. A., WILLNER, D., HUGENHOLTZ, P., RABAEY, K. & BUIE, C. R. 2013. Dielectrophoresis-Based Discrimination of Bacteria at the Strain Level Based on Their Surface Properties. *PLoS ONE*, 8, e76751.
- 13 BRASCHLER, T., DEMIERRE, N., NASCIMENTO, E., SILVA, T., OLIVA, A. G. & RENAUD, P. 2008. Continuous separation of cells by balanced dielectrophoretic forces at multiple frequencies. *Lab on a Chip*, 8, 280-286.

- 14 BROWN, L., KOERNER, T., HORTON, J. H. & OLESCHUK, R. D. 2006. Fabrication and characterization of poly(methylmethacrylate) microfluidic devices bonded using surface modifications and solvents. *Lab Chip*, 6, 66-73.
- 15 CASTELLARNAU, M., ERRACHID, A., MADRID, C., JUÁREZ, A. & SAMITIER, J. 2006. Dielectrophoresis as a Tool to Characterize and Differentiate Isogenic Mutants of *Escherichia coli*. *Biophysical Journal*, 91, 3937-3945.
- 16 CHANG, H. C. & YEO, L. Y. 2010. *Electrokinetically driven microfluidics and nanofluidics*, Cambridge ; New York, Cambridge University Press.
- 17 CHIANG, T., ASSIDJO, N. E. & CARDOT, P. J. P. 2000. Sedimentation field-flow-fractionation: emergence of a new cell separation methodology. *Talanta*, 51, 835-847.
- 18 CHOI, S. & PARK, J.-K. 2005. Microfluidic system for dielectrophoretic separation based on a trapezoidal electrode array. *Lab on a Chip*, 5, 1161-1167.
- 19 CHOU, C.-F., MORGAN, M., ZENHAUSERN, F., PRINZ, C. & AUSTIN, R. 2002. Electrodeless Dielectrophoretic Trapping and Separation of Cells. In: BABA, Y., SHOJI, S. & VAN DEN BERG, A. (eds.) *Micro Total Analysis Systems 2002*. Springer Netherlands.
- 20 CUMMINGS, E. B. & SINGH, A. K. 2003. Dielectrophoresis in Microchips Containing Arrays of Insulating Posts: Theoretical and Experimental Results. *Analytical Chemistry*, 75, 4724-4731.
- 21 DAINIAK, M. B., KUMAR, A., GALAEV, I. Y. & MATTIASSON, B. 2007. Methods in cell separations. *Adv Biochem Eng Biotechnol*, 106, 1-18.
- 22 DEWILDT, R. M. T., STEENBAKKERS, P. G., PENNING, A. H. M., VANDENHOOGEN, F. H. J., VANVENROOIJ, W. J. & HOET, R. M. A. 1997. A new method for the analysis and production of monoclonal antibody fragments originating from single human B cells. *Journal of Immunological Methods*, 207, 61-67.
- 23 EDELMAN, G. M., RUTISHAUSER, U. & MILLETTE, C. F. 1971. Cell Fractionation and Arrangement on Fibers, Beads, and Surfaces. *Proceedings of the National Academy of Sciences of the United States of America*, 68, 2153-&.
- 24 EL-ALL, J., SORGER, P. K. & JENSEN, K. F. 2006. Cells on chips. *Nature*, 442, 403-411.
- 25 FUKUDA, J., SAKAI, Y. & NAKAZAWA, K. 2006. Novel hepatocyte culture system developed using microfabrication and collagen/polyethylene glycol microcontact printing. *Biomaterials*, 27, 1061-1070.
- 26 GAGNON, Z. & CHANG, H. C. 2005. A wire loop design for convection-enhanced dielectrophoretic bioparticle trapping. *ICMM 2005: 3rd International Conference on Microchannels and Minichannels, Pt B*, 473-480.
- 27 GAWAD, S., SCHILD, L. & RENAUD, P. 2001. Micromachined impedance spectroscopy flow cytometer for cell analysis and particle sizing. *Lab on a Chip*, 1, 76-82.

- 28 GIVAN, A. L. 2004. Flow cytometry: an introduction. *Methods Mol Biol*, 263, 1-32.
- 29 GORRE-TALINI, L., JEANJEAN, S. & SILBERZAN, P. 1997. Sorting of Brownian particles by the pulsed application of an asymmetric potential. *Physical Review E*, 56, 2025-2034.
- 30 GREEN, N. G. & MORGAN, H. 1998. Dielectrophoresis of Submicrometer Latex Spheres. 1. Experimental Results. *The Journal of Physical Chemistry B*, 103, 41-50.
- 31 GREEN, N. G. & MORGAN, H. 1999. Dielectrophoresis of submicrometer latex spheres. 1. Experimental results. *Journal of Physical Chemistry B*, 103, 41-50.
- 32 GRIMNES, S. & MARTINSEN, Ø. G. 2008. *Bioimpedance and bioelectricity basics*, Amsterdam ; Boston, Elsevier Academic Press.
- 33 GRODZINSKY, A. J. & FRANK, E. H. 2011. *Fields, forces, and flows in biological systems*, London ; New York, Garland Science.
- 34 HAWKINS, B. G. & KIRBY, B. J. 2010. Electrothermal flow effects in insulating (electrodeless) dielectrophoresis systems. *Electrophoresis*, 31, 3622-3633.
- 35 HAWKINS, B. G., SMITH, A. E., SYED, Y. A. & KIRBY, B. J. 2007. Continuous-flow particle separation by 3D Insulative dielectrophoresis using coherently shaped, dc-biased, ac electric fields. *Anal Chem*, 79, 7291-300.
- 36 HERZENBERG, L. A., PARKS, D., SAHAF, B., PEREZ, O., ROEDERER, M. & HERZENBERG, L. A. 2002. The history and future of the fluorescence activated cell sorter and flow cytometry: A view from Stanford. *Clinical Chemistry*, 48, 1819-1827.
- 37 HOEBER, T. W. & HOCHMUTH, R. M. 1970. Measurement of Red Cell Modulus of Elasticity by in-Vitro and Model Cell Experiments. *Journal of Basic Engineering*, 92, 604-&.
- 38 HU, Q., JOSHI, R. P. & BESKOK, A. 2009. Model study of electroporation effects on the dielectrophoretic response of spheroidal cells. *Journal of Applied Physics*, 106, -.
- 39 HUANG, Y., HOLZEL, R., PETHIG, R. & WANG, X. B. 1992. Differences in the AC electrodynamics of viable and non-viable yeast cells determined through combined dielectrophoresis and electrorotation studies. *Phys Med Biol*, 37, 1499-517.
- 40 IRIMAJIRI, A., HANAI, T. & INOUE, A. 1975. Dielectric Properties of Synaptosomes Isolated from Rat-Brain Cortex. *Biophysics of Structure and Mechanism*, 1, 273-283.
- 41 JACKSON, J. D. 1999. *Classical electrodynamics*, New York, Wiley.
- 42 JENSEN, M. F., NOERHOLM, M., CHRISTENSEN, L. H. & GESCHKE, O. 2003. Microstructure fabrication with a CO2 laser system: characterization and fabrication of cavities produced by raster scanning of the laser beam. *Lab on a Chip*, 3, 302-307.
- 43 JO, B. H., VAN LERBERGHE, L. M., MOTSEGOOD, K. M. & BEEBE, D. J. 2000. Three-dimensional micro-channel fabrication in polydimethylsiloxane (PDMS) elastomer. *Journal of Microelectromechanical Systems*, 9, 76-81.

- 44 KALE, A., PATEL, S., HU, G. Q. & XUAN, X. C. 2013. Numerical modeling of Joule heating effects in insulator-based dielectrophoresis microdevices. *Electrophoresis*, 34, 674-683.
- 45 KANG, K. H., KANG, Y., XUAN, X. & LI, D. 2006. Continuous separation of microparticles by size with direct current-dielectrophoresis. *Electrophoresis*, 27, 694-702.
- 46 KANG, K. H., XUAN, X. C., KANG, Y. J. & LI, D. Q. 2006. Effects of dc-dielectrophoretic force on particle trajectories in microchannels. *Journal of Applied Physics*, 99.
- 47 KANG, Y. J., LI, D. Q., KALAMS, S. A. & EID, J. E. 2008. DC-Dielectrophoretic separation of biological cells by size. *Biomedical Microdevices*, 10, 243-249.
- 48 KLANK, H., KUTTER, J. P. & GESCHKE, O. 2002. CO₂-laser micromachining and back-end processing for rapid production of PMMA-based microfluidic systems. *Lab on a Chip*, 2, 242-246.
- 49 LAPIZCO-ENCINAS, B. H., DAVALOS, R. V., SIMMONS, B. A., CUMMINGS, E. B. & FINTSCHENKO, Y. 2005. An insulator-based (electrodeless) dielectrophoretic concentrator for microbes in water. *Journal of Microbiological Methods*, 62, 317-326.
- 50 LAPIZCO-ENCINAS, B. H., SIMMONS, B. A., CUMMINGS, E. B. & FINTSCHENKO, Y. 2004. Dielectrophoretic concentration and separation of live and dead bacteria in an array of insulators. *Analytical Chemistry*, 76, 1571-1579.
- 51 LAPIZCO-ENCINAS, B. H., SIMMONS, B. A., CUMMINGS, E. B. & FINTSCHENKO, Y. 2004. Insulator-based dielectrophoresis for the selective concentration and separation of live bacteria in water. *Electrophoresis*, 25, 1695-1704.
- 52 LEWPIRIYAWONG, N., KANDASWAMY, K., YANG, C., IVANOV, V. & STOCKER, R. 2011. Microfluidic Characterization and Continuous Separation of Cells and Particles Using Conducting Poly(dimethyl siloxane) Electrode Induced Alternating Current-Dielectrophoresis. *Analytical Chemistry*, 83, 9579-9585.
- 53 LEWPIRIYAWONG, N. & YANG, C. 2012. AC-dielectrophoretic characterization and separation of submicron and micron particles using sidewall AgPDMS electrodes. *Biomicrofluidics*, 6, -.
- 54 LEWPIRIYAWONG, N., YANG, C. & LAM, Y. C. 2010. Continuous sorting and separation of microparticles by size using AC dielectrophoresis in a PDMS microfluidic device with 3-D conducting PDMS composite electrodes. *ELECTROPHORESIS*, 31, 2622-2631.
- 55 LI, S. B., LI, M., HUI, Y. S., CAO, W. B., LI, W. H. & WEN, W. J. 2013. A novel method to construct 3D electrodes at the sidewall of microfluidic channel. *Microfluidics and Nanofluidics*, 14, 499-508.
- 56 MAXWELL, J. C. 2010. *A Treatise on Electricity and Magnetism*, Cambridge University Press.

- 57 MCCORMICK, R. M., NELSON, R. J., ALONSOAMIGO, M. G., BENVEGNI, J. & HOOPER, H. H. 1997. Microchannel electrophoretic separations of DNA in injection-molded plastic substrates. *Analytical Chemistry*, 69, 2626-2630.
- 58 MORGAN, H. & GREEN, N. G. 2003. *AC electrokinetics: colloids and nanoparticles*, Baldock, UK, Research Studies Press Limited.
- 59 O'BRIEN, R. W. 1986. The high-frequency dielectric dispersion of a colloid. *Journal of Colloid and Interface Science*, 113, 81-93.
- 60 O'KONSKI, C. T. 1960. ELECTRIC PROPERTIES OF MACROMOLECULES. V. THEORY OF IONIC POLARIZATION IN POLYELECTROLYTES. *The Journal of Physical Chemistry*, 64, 605-619.
- 61 PERTOFT, H. 2000. Fractionation of cells and subcellular particles with Percoll. *Journal of Biochemical and Biophysical Methods*, 44, 1-30.
- 62 POHL, H. A. & HAWK, I. 1966. Separation of Living and Dead Cells by Dielectrophoresis. *Science*, 152, 647-&.
- 63 PRETLOW, T. G., PRETLOW, T.P. (ed.) 1987. *Cell separation: methods and selective applications*, New York: Academic.
- 64 RAMOS, A., MORGAN, H., GREEN, N. G. & CASTELLANOS, A. 1998. Ac electrokinetics: a review of forces in microelectrode structures. *Journal of Physics D-Applied Physics*, 31, 2338-2353.
- 65 SAFARIK, I. & SAFARIKOVA, M. 1999. Use of magnetic techniques for the isolation of cells. *J Chromatogr B Biomed Sci Appl*, 722, 33-53.
- 66 SAVILLE, D. A., BELLINI, T., DEGIORGIO, V. & MANTEGAZZA, F. 2000. An extended Maxwell-Wagner theory for the electric birefringence of charged colloids. *Journal of Chemical Physics*, 113, 6974-6983.
- 67 SCHALLER, T., BOHN, L., MAYER, J. & SCHUBERT, K. 1999. Microstructure grooves with a width of less than 50 μm cut with ground hard metal micro end mills. *Precision Engineering*, 23, 229-235.
- 68 SCHWINGER, J. 1998. *Classical electrodynamics*, Reading, Mass., Perseus Books.
- 69 SEIDL, J., KNUECHEL, R. & KUNZ-SCHUGHART, L. A. 1999. Evaluation of membrane physiology following fluorescence activated or magnetic cell separation. *Cytometry*, 36, 102-11.
- 70 SHAFIEE, H., SANO, M. B., HENSLEE, E. A., CALDWELL, J. L. & DAVALOS, R. V. 2010. Selective isolation of live/dead cells using contactless dielectrophoresis (cDEP). *Lab on a Chip*, 10, 438-445.
- 71 SNAKENBORG, D., KLANK, H. & KUTTER, J. P. 2004. Microstructure fabrication with a CO₂ laser system. *Journal of Micromechanics and Microengineering*, 14, 182-189.

- 72 SRIDHARAN, S., ZHU, J. J., HU, G. Q. & XUAN, X. C. 2011. Joule heating effects on electroosmotic flow in insulator-based dielectrophoresis. *Electrophoresis*, 32, 2274-2281.
- 73 SUN, T., HOLMES, D., GAWAD, S., GREEN, N. G. & MORGAN, H. 2007. High speed multi-frequency impedance analysis of single particles in a microfluidic cytometer using maximum length sequences. *Lab on a Chip*, 7, 1034-1040.
- 74 THWAR, P. K., LINDERMAN, J. J. & BURNS, M. A. 2007. Electrodeless direct current dielectrophoresis using reconfigurable field-shaping oil barriers. *ELECTROPHORESIS*, 28, 4572-4581.
- 75 TSUKAHARA, S., SAKAMOTO, T. & WATARAI, H. 2000. Positive dielectrophoretic mobilities of single microparticles enhanced by the dynamic diffusion cloud of ions. *Langmuir*, 16, 3866-3872.
- 76 VOLDMAN, J., GRAY, M. L., TONER, M. & SCHMIDT, M. A. 2002. A microfabrication-based dynamic array cytometer. *Analytical Chemistry*, 74, 3984-3990.
- 77 WAGNER, K. 1914. Erklärung der dielektrischen Nachwirkungsvorgänge auf Grund Maxwell'scher Vorstellungen. *Archiv für Elektrotechnik*, 2, 371-387.
- 78 WHITESIDES, G. M., OSTUNI, E., TAKAYAMA, S., JIANG, X. Y. & INGBER, D. E. 2001. Soft lithography in biology and biochemistry. *Annual Review of Biomedical Engineering*, 3, 335-373.
- 79 YANG, F., YANG, X., JIANG, H., BULKHAULTS, P., WOOD, P., HRUSHESKY, W. & WANG, G. 2010. Dielectrophoretic separation of colorectal cancer cells. *Biomicrofluidics*, 4, -.
- 80 ZHAO, H. 2011. Double-layer polarization of a non-conducting particle in an alternating current field with applications to dielectrophoresis. *ELECTROPHORESIS*, 32, 2232-2244.
- 81 ZHU, J., TZENG, T.-R., HU, G. & XUAN, X. 2009. DC dielectrophoretic focusing of particles in a serpentine microchannel. *Microfluidics and Nanofluidics*, 7, 751-756.
- 82 ZHU, J., TZENG, T.-R. J. & XUAN, X. 2010. Continuous dielectrophoretic separation of particles in a spiral microchannel. *ELECTROPHORESIS*, 31, 1382-1388.
- 83 ZHU, J. & XUAN, X. 2009. Dielectrophoretic focusing of particles in a microchannel constriction using DC-biased AC electric fields. *ELECTROPHORESIS*, 30, 2668-2675.
- 84 ZHU, J. & XUAN, X. 2009. Particle electrophoresis and dielectrophoresis in curved microchannels. *Journal of Colloid and Interface Science*, 340, 285-290.